

DEM analyses of cemented granular fault gouges at the onset of seismic sliding: peak strength, development of shear zones and kinematics

N. Casas^{1,2}, G. Mollon¹, and A. Daouadji²

¹ Univ. Lyon, INSA-Lyon, CNRS UMR5259, LaMCoS, F-69621, France.

5 ² Univ Lyon, INSA Lyon, GEOMAS, EA7495, 69621 Villeurbanne, France

Nathalie Casas (nathalie.casas@insa-lyon.fr)

Key Points:

- The increase of cementation within the gouge shows an evolution from ductile to brittle behavior and different failure patterns.
- 10 • Shear fracturing of a fault gouge needs a critical dilatancy and dense cemented material presents a double weakening shape.
- Strength ratio of a cemented gouge cannot be predicted from Mohr-Coulomb criteria, because of the stress state and kinematic constraints.

15 Plain Language Summary

Fault zones usually present a granular layer (i.e. fragments of the rock) between sliding rocks that plays a key role in the initiation and stability of earthquakes. In this study, we use numerical models (with realistic sizes and shapes of grains composing the layer), to better understand the link between properties of this layer and the slip behavior of a fault. When the fault is not
20 sliding, mineral cementation can form around grains and thus changes fault properties. We test here different percentages of this cementation and different porosities for the initial state of the fault, and see their influence on sliding fault behavior. For the investigated data range, three types of cemented material are highlighted with an evolution of the failure pattern with the increase of the cementation (from ductile to brittle). These results are compared to real data for
25 intact or layered rocks in terms of frictional strength, cohesion, and failure patterns. We also find that the strength of a cemented fault cannot be predicted from Mohr-Coulomb criteria because of constraints of the associated fault zone.

Abstract

Fault zones usually present a granular gouge, coming from the wear material of previous slips. This layer contributes to friction stability and plays a key role in the way elastic energy is released during sliding. Considering a mature fault gouge with a change in the percentage of mineral cementation between particles, we aim to understand the influence of interparticle bonds on slip mechanisms by employing the Discrete Element Method. We consider a direct shear model without fluid in 2D, based on a granular sample with realistic grain sizes and shapes. Focusing on the physics of contacts inside the granular gouge, we explore contact interactions and effective friction coefficient within the fault. Brittleness is enhanced with cementation and even more with dense materials. For the investigated data range, three types of cemented material are highlighted: a mildly cemented material (Couette flow, no cohesion), a cemented material with agglomerates of cemented particles changing the granular flow and acting on slip weakening mechanisms (Riedel shear bands R1), and an ultra-cemented material behaving as a brittle material (with several Riedel bands followed by shear-localization). Effective friction curves present double weakening shapes for dense samples with enough cementation. We find that effective friction of a cemented fault cannot be predicted from Mohr-Coulomb criteria because of the specific stress state and kinematic constraints of the fault zone.

1. Introduction

During an earthquake, frictional sliding releases the stresses accumulated in the pre-stressed surrounding medium. The fault gouge identified as the wear material of previous slips contributes to friction stability (Marone & Scholz, 1988) and plays an important role in the sudden energy release at the onset of seismic sliding (C. Sammis et al., 1987). The number and amplitudes of successive slips occurring within the gouge reduce the size of particles towards a fractal distribution, which also reduces pore spaces [(C. G. Sammis & Biegel, 1989), (Blenkinsop, 1991), (Muto et al., 2015)]. This particle size distribution can be explained by grain breakage theory [(Daouadji et al., 2001), (Daouadji & Hicher, 2010)]. Within a mature fault gouge, mineral cementation coming from rock dissolution, melting, or other processes derived from previous slips, can fill remaining pore spaces between particles and change the global state of cohesion (Philit et al., 2018). (Lade & Overton, 1989) showed that, for low confining pressures, the increase of cementation and the associated tensile strength lead to an enhancement of effective friction coefficient. This phenomenon gives birth to a new, stronger granular material combining its history, the state of initial density (i.e. porosity within the

sample), and cementation (Schellart, 2000). During gouge shearing, at low confining pressure, the breakage of cement bridges between particles enhances local kinematic freedom and allows grains reorganization, such as the formation of shear plane failures and global dilation (Tengattini et al., 2014).

A wide range of gouge characteristics (mineralogy, particle size, friction...) and constrained environment (pressure, slip velocity...) are believed to influence, if not control, a large part of slip mechanisms. Such gouge parameters have been studied in the literature from Lab or in-situ points of view [(Byerlee & Brace, 1968), (C. Sammis et al., 1987), (Biegel et al., 1989), (Marone & Scholz, 1989), (Mair & Marone, 1999), (Anthony & Marone, 2005)] and also numerically by the mean of Discrete Element Modelling (DEM) [(Morgan & Boettcher, 1999), (Morgan, 1999), (Guo & Morgan, 2004), (Da Cruz et al., 2005), (Cho et al., 2008), (Zhao et al., 2012), (Gao et al., 2018)]. Cementation and its influence on slip behavior are less represented in the field of fault mechanics. It may be due to the difficulty to introduce and control a cemented gouge material in experiments, but also to their atypical behavior introducing local force chains within the gouge. That is the reason why Discrete Element Modelling (DEM) seems to be a good way to complete knowledge on cemented materials and their influence on slip mechanisms within the gouge in terms of strength, slip weakening, and failure patterns. In DEM, the cementation can be schematized by cohesive and breakable bonds between particles. Bonded Particle Models are often used to represent cohesive laws within granular rocks [(Potyondy & Cundall, 2004), (Cho et al., 2007)] or to represent cementation [(Estrada et al., 2010), (Jiang et al., 2013), (Das et al., 2014), (Tengattini et al., 2014)]. The present study proposes to combine modern simulation technics for cemented granular material with fault mechanics and to investigate the initiation of granular fault gouge shearing. As most DEM studies are modelling circular shapes of particles, we also propose to model angular shapes of grains in order to have a more realistic behavior.

Slip weakening literature reports a large range of phenomena occurring during faulting. They are mainly observed under high pressure and velocity, within a very thin slipping zone, and need a certain amount of sliding before occurring. The temperature rise can lead to melting [(Giulio Di Toro et al., 2006) & (Niemeijer et al., 2011)] or fluid pressurization (J. R. Rice, 2006). These heating processes are related to a large mechanical work rate within the slip zone (G Di Toro et al., 2011) and are responsible for thermal weakening. The well-known critical slip distance D_c is the slip distance corresponding to a decrease in frictional strength (and be part of rate and state friction laws (Marone, 1998)), and is in the order 1 to 10 m for natural

earthquakes and from 10^{-5} to 10^{-3} m for lab experiments at low slip velocity (Marone & Kilgore, 1993). Another contribution to weakening is related to simple fracture mechanics and slipping zone. The mechanism by which frictional resistance drops with sliding is known as "slip weakening" and may be the cause of unstable sliding, releasing energy within the system in the form of high slip rate and stresses across the fault. It is thus influenced by both the roughness of the fault surface and the thickness of the gouge (Marone & Kilgore, 1993). The main slipping zone can contain cohesive or non-cohesive wear material (J. Rice & Cocco, 2002), and a micrometer-millimeter scale slip distance is observed. In this paper, we restrict our focus on this immediate slip weakening and disregard all thermal effects, which are supposed to happen later after a certain amount of slip.

The objective of this paper is to establish a link between the micro-mechanical and structural properties of a cemented gouge layer, and its rheological behavior under shearing. Varying the percentage of cementation within the gouge, for different initial porosities, leads to a wide range of mechanical behaviors that we can compare to fracture mechanics theory. Section two introduces the numerical method and the fault segment model in 2D ($2 \times 20 \text{ mm}^2$) involving two rough surfaces representing the rock walls separated by the cemented granular gouge. This paper proposes to use DEM on angular and faceted grains as we can find in real granular fault gouge. Focusing on physics of contacts inside the granular medium, we explore strength evolution, gouge kinematics, and force chains within the gouge in a third section. We aim in this section to study the effect of cementation and initial porosity on mechanical behaviors and kinematics of shear bands. The last section offers a discussion on new insights and relations between cementation within the gouge, shear localization, and relevance of Mohr-Coulomb theory for fault models.

2. Numerical framework and sample generation

To simulate a cohesive granular fault gouge, a 2D model is implemented in the framework of Discrete Element Modelling (DEM) in the software MELODY. This software allows simulating angular and faceted grain shapes with three steps of contact detection. This section introduces the general methods and initial setup used for DEM modeling. More information about contact algorithms and solver are available in [(Mollon, 2018b) & (Mollon, 2016)].

2.1. Discrete Element Modelling with angular and faceted grains

Since DEM was first proposed by (Cundall & Strack, 1979), it has been applied several times to the simulation of micro-scale behaviors inside fault zones [(Morgan & Boettcher, 1999),

(Morgan, 1999), (Guo & Morgan, 2004), (Da Cruz et al., 2005), (Cho et al., 2008), (Zhao et al., 2012), (Gao et al., 2018)]. Each particle has its own movement and trajectory, driven by Newton's laws of motion. The movement is controlled by user-defined and physics-based contact interactions and constitutive laws inside the sample. Since the contour of each grain is discretized by a piecewise linear frontier with nodes and segments, each contact considered in the code concerns a given node from a grain A and a given segment from a grain B. From this node and this segment, we can at any moment compute a normal gap δ_n (obtained by projecting the node on the segment) and a tangential gap δ_t (integrated in time based on the history of the relative motions of the node and the segment in the tangential direction). δ_n can be either negative (i.e. there is a small interpenetration between the grains) or positive (i.e. there is a separation distance between the grains). This contact algorithm is described in more details in (Mollon, 2018a). To control overlapping, a contact stiffness is introduced in the normal and tangential directions (k_n and k_t).

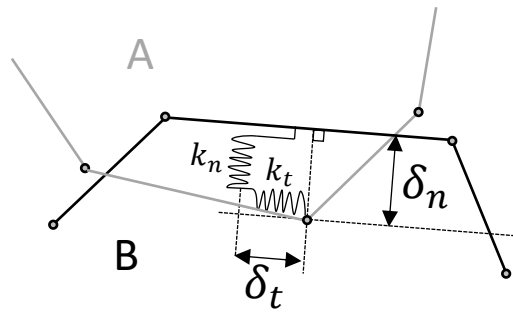


Figure 1. Sketch of a typical contact between two grains A and B. k_n and k_t are respectively the normal stiffness and the tangential stiffness and δ_n and δ_t are the associated gaps used to control interpenetrations between particles.

The code used for simulations, MELODY 2D (Multibody ELe ment-free Open code for DYnamic simulation), is a C++ code allowing to simulate any kind of granular media. In contrast with conventional codes, it can deal with any 2D shape and behavior of particles, from rigid circular to highly compliant angular grains (this latter case is outside of the strict DEM framework, and uses a Multibody Meshfree Approach). One of the objectives of this paper is to propose new results for sheared granular gouge with shapes of particles closer to reality (angular and faceted grains). More details on software and DEM are available in (*Supporting Information S1 and S2*) and the detailed equations used for cemented material are presented in the next section.

2.2. Bonded particles within the gouge

In this paper, we consider a fault zone that has already been sheared in previous slip episodes, and which became mature enough to observe mineral cementation between particles. This cementation cannot be explicitly simulated with DEM, as it could fill all the pore spaces within the gouge, but can be represented in a simplified manner by considering breakable cohesive bonds between particles. A “Bonded Mohr-Coulomb” law is therefore applied. This contact law is close to the Bonded-Particle-Model (BPM) from (Potyondy & Cundall, 2004) and presents two main status (intact or broken) described below:

(a) After compaction and before shearing, all contacts for which $\delta_n < (\delta_{detection} = C_{num}/k_n)$, where k_n is the contact stiffness and C_{num} is the numerical cohesion, receive the status “intact” (Figure 2 – a).

↳ If the contact is “intact”, the following contact stresses are computed based on a purely elastic contact law:

$$\sigma_n = k_n \delta_n \quad (2.2.1)$$

$$\sigma_t = k_t \delta_t \quad (2.2.2)$$

↳ If $[\sigma_n \text{ or } abs(\sigma_t)]$ exceeds the prescribed value of cohesion C_{num} , the status of the contact is updated to “broken” (Figure 2 – b).

(b) If the contact is “broken”, (Figure 2 – b), either because it is a former intact bond or because it is newly created by grains motions at any time in the simulation, the following contact stresses are computed based on a purely frictional contact law:

$$if (\delta_n > 0) \rightarrow \sigma_n = \sigma_t = 0 \quad (2.2.3)$$

$$if (\delta_n < 0) \rightarrow \left\{ \begin{array}{l} \sigma_n = k_n \delta_n \\ \sigma_t = min(k_t \delta_t, \mu_{num} \sigma_n) \end{array} \right. \quad (2.2.4)$$

$$\sigma_t = min(k_t \delta_t, \mu_{num} \sigma_n) \quad (2.2.5)$$

Where μ_{num} is the inter-particle friction coefficient.

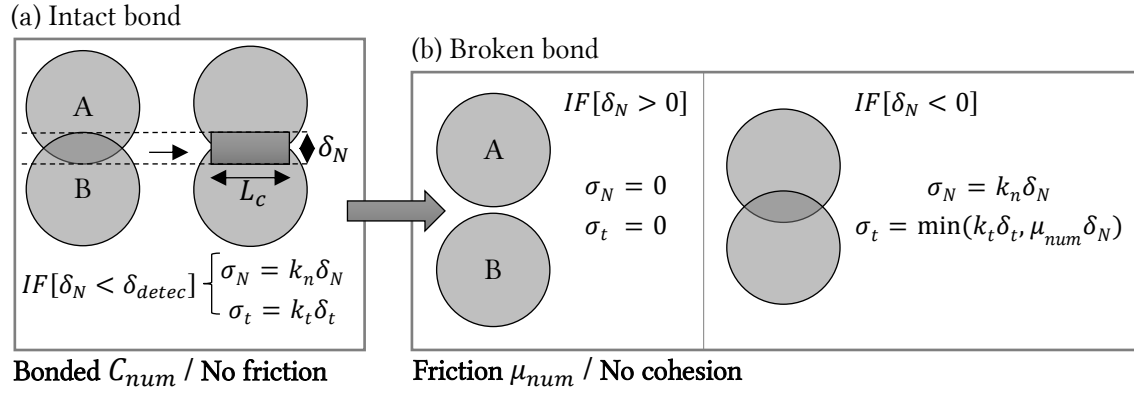


Figure 2. (a) Intact bond. Initialization of the contact law. A cohesive law links all grains in contact. The bond corresponds to a constant pressure to maintain particles in contact (Pa). (b) Broken bond. When the force applied to the particles becomes higher than the cohesive strength, the bond is broken. The contact becomes cohesionless and follows a classical Mohr-Coulomb law with inter-particle friction only. Broken contacts cannot be cohesive again and this induces an augmentation of broken bonds during the shearing.

From these stresses, the associated contact forces (in the normal and tangential direction, as well as the associated torque) are computed on each grain, by considering that contact stresses act on a contact length L_c (equal to the sum of half-lengths of the segments around contact nodes in grain A):

$$F_n = L_c \delta_n \quad (2.2.6)$$

$$F_t = L_c \delta_t \quad (2.2.7)$$

These laws are completed by a classical viscous dashpot to dissipate kinetic energy by contact damping and to stabilize the simulation (γ_n & γ_t).

The numerical cohesion C_{num} considered in the code cannot be directly related to real cementation in rocks and does not bear much physical signification by itself. A good way to associate a quantitative description to this numerical parameter is to define an associated level of cementation. In the initial state of our model, each cohesive bond between any pair of contacting grains requires a certain amount of mechanical energy for breaking. This energy is related to its tensile and tangential stiffnesses, to its tensile and tangential strengths, and to its contact length L_c . To clarify the total amount of energy that would be needed in order to break all the initial cohesive bonds, we normalize it with respect to a representative energy. This energy corresponds to a surface energy of 62J/m² which was reported for the Chilhowee quartzite and considered as an upper limit for rock surface energy by (Friedman et al., 1972). We apply this surface energy on the whole external surface of all grains present in the simulation (a unit length is considered in the third dimension for any necessary purpose), and

consider that this amount of energy corresponds to a complete cementation of the gouge layer. Hence, any initial state of cementation effectively introduced in the numerical samples by the means of the numerical cohesion C_{num} can be defined as a certain percentage of this complete cementation (*details of calculi in Supporting Information S3*). Thus, a simulation case with a cementation of $P_{cem}=20\%$ is to be interpreted in the sense that, in its initial state, the energy needed to break all its bonds is equal to 20% of that of the fully cemented case.

2.3. Granular fault gouge sample

Mineral grains morphologies can be very diverse, but granular gouges generated by comminution are expected to exhibit rather rough and angular shapes [(Olgaard & Brace, 1983), (An & Sammis, 1994), (Lin, 1999)]. Many studies [(Mair et al., 2002), (Nouguier-lehon et al., 2003), (Anthony & Marone, 2005)] have shown that using angular and faceted shapes instead of circular grains led to higher friction coefficients and different global behaviors. For 3D laboratory experiments with real grains, steady-state effective friction is usually around 0.6 (Mair et al., 2002), in opposition to spherical particles with effective friction that rarely exceeds 0.45. Because of their invariance by rotation, smooth spherical shapes tend to roll to accommodate deformation of the grain assembly whereas interlocking between angular grains tends to promote dilation. It was also shown recently that mechanical effects of grains surface roughness can only be mimicked by intergranular friction to a certain extent, and that proper modeling of the shear behavior of granular samples requires realistic shapes (Mollon et al., 2020). To be closer to real behavior, angular and faceted particles are employed in this study. However, to validate the importance to model these shapes of grains compared to circular shapes, and validate our model with literature, two samples were implemented: one with angular and faceted particles (the one used for the study) and another one with circular grains. This second sample was then discarded, as explained in (*Supporting Information S4*).

The Matlab package Packing2D is employed to create a realistic granular sample. It is based on a Fourier-Voronoi method and generates a set of angular and faceted grains with user-defined size distribution and control on key morphological descriptors (such as elongation, circularity, and roundness). This control is performed by choosing a Fourier spectrum that quantifies the frequencies and amplitudes of the grain surface asperities. More information is available in (Mollon & Zhao, 2012). Since the morphological descriptors of the grains of granular gouges may vary significantly between faults, we calibrate our spectrum by visual comparison with published pictures of real gouges (Figure 3 (a) – (b)).

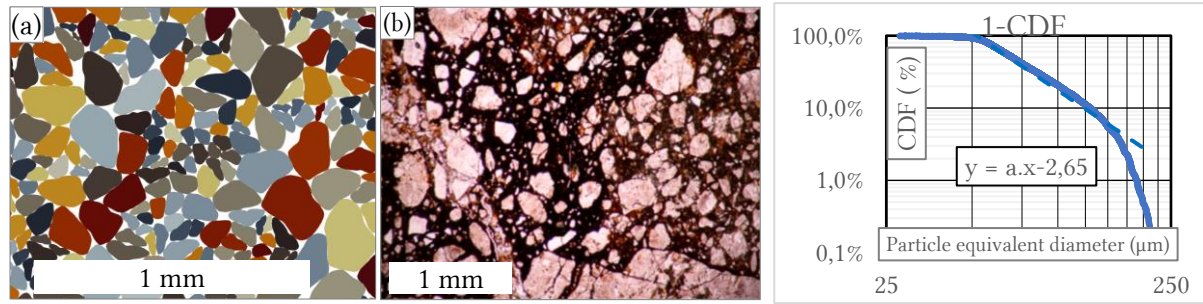


Figure 3. (a) Zoom on a granular sample generated with packing2D, with angular and faceted shapes, and compacted in MELODY2D (b) Quartz, photomicrograph (crossed polars) of ATTL fault gouge from (Muto et al., 2015). (c) Size distribution of the synthetic sample.

The thickness of the shearing zone should be between 1 and 5 mm (J. Rice & Cocco, 2002). We create a 2mm-thick granular fault gouge (before compaction), resulting in 1.7 mm after compaction, and determine what length is needed to obtain a Representative Surface Element (RSE), (*Supporting Information S5*). A gouge of 2 x 20 mm² is found to be satisfactory and falls within the same order of magnitude as previous studies [(Ferdowsi, 2014) & (Dorostkar et al., 2017)]. A fractal size distribution is chosen to fit with the literature on granular gouge composition, [(Olgaard & Brace, 1983), (Blenkinsop, 1991), (Billi & Storti, 2004), (Billi, 2005), (Muto et al., 2015)] with a fractal dimension factor D close to 2.6. The gouge with angular grains is composed of 4960 particles with a corresponding equivalent diameter in the range of 28 – 226 μm (average value of 81 μm) and a (D_{50}) equal to 70 μm (Figure 3 – c).

2.4. Numerical setup

Figure 4 presents the DEM model of the granular fault gouge, with rock walls at the top and bottom sides of the granular sample. Contact surfaces of rock walls are sinusoidal to introduce a certain roughness and avoid wall-slip effects since we want to ensure that slip accommodation takes place within the gouge. Inter-particle friction is equal to 1 at the contact interface between walls and particles to make sure that the motion is fully coupled at the wall-grains transition. For inter-particle contacts μ_{num} , friction is set to 0.5. This value is often used in DEM gouge experiments and is in the range of inter-particle friction found for two frictional particles in contacts [(Sandeep & Senetakis, 2019) & (Kasyap & Senetakis, 2020)].

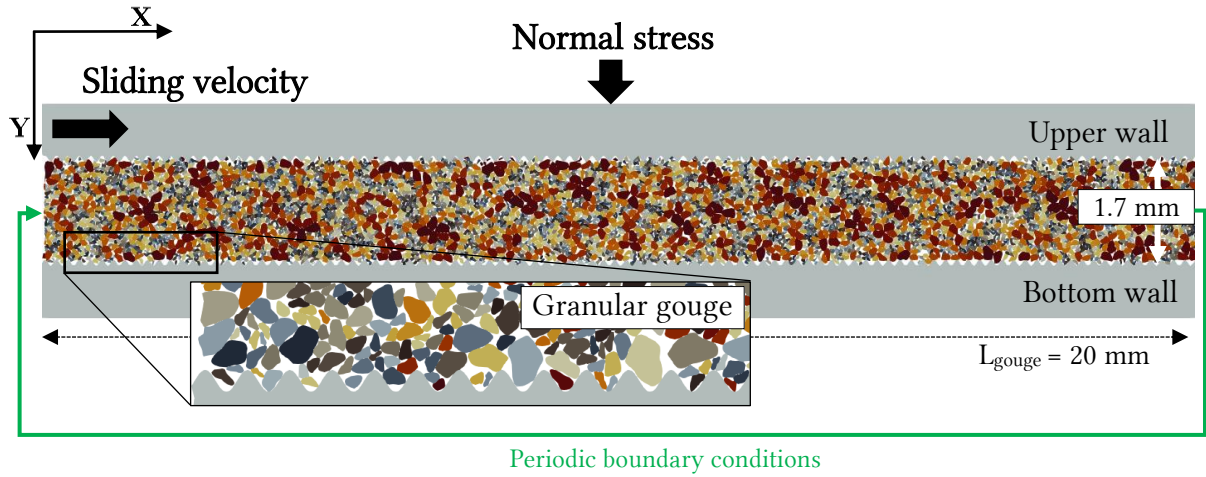


Figure 4. DEM model of a granular fault gouge, 4960 angular particles in a 1.7x20mm domain.

The lower wall is fixed, while a normal stress of 40 MPa and a sliding velocity are applied on the upper rock wall. Gravity is ignored in the model, assuming that the fault can be oriented in a wide range of directions, and that gravity forces are negligible compared to those related to normal and deviatoric stresses applied on the gouge. Periodic boundary conditions are present on both right- and left-hand sides of the sample to maintain the continuity of the movement at large slips. The movement of the upper rock wall in the y-direction remains free to allow gouge dilatancy.

A dry contact model is considered here, to investigate cementation and porosity influences alone, without fluid. Fault gouge and rock walls are considered rigid with a constant numerical stiffness of 10^{15} N/m³ used to limit interpenetration between grains while mimicking the local deformation of the grains in the contact vicinity (section 2.1 and 2.2). This constant value was chosen to obtain the overall deformability of the sample of the same order of magnitude as the one for bulk granite or shearing modulus (≈ 10 -25 MPa depending on initial porosity, see section 3.1). The tangential and normal numerical stiffnesses are equals in this model and grain comminution is disregarded. In this study, we choose to simulate a realistic volumetric mass of 2600 kg/m³ for particles, leading to an appropriate time step for these simulations of 10^{-9} s. An explicit solver is used (Symplectic Euler scheme), to integrate in time the motion of each body. The first simulation stage consists of compacting the gouge to obtain a mechanically stable packing of grains with a controlled granular density. We consider two different initial porosities for this study, ($P_{pore} = 16\%$) for mid-dense samples and, ($P_{pore} = 11\%$) for dense samples (Supporting Information S6).

After compaction and stabilization, the contact law between grains is modified by the introduction of cohesive bonds between particles (see the previous subsection) and a 1 m/s

slipping rate is applied on the upper rock wall. This high velocity allows the simulations to run in a reasonable amount of time while avoiding disturbing inertial effects since the dimensionless inertial number, in that case, is close to 10^{-3} (i.e. quasi-static dense granular flow according to (Da Cruz et al., 2005)).

Table 1: Numerical setup and properties

Property	Associated variable	Value
Normal stress	σ_n	40 MPa
Shear velocity	V	1 m/s
Rock density	ρ_r	2600 grains Kg/m ³
Contact stiffness	$k_n \& k_t$	10^{15} Pa/m
Cohesive bond strength	C_{num}	0 – 2500 MPa
Percentage of cementation	P_{cem}	0% - 100%
Percentage of initial porosity	P_{pore}	11% & 16%
Inter-particle friction	μ_{num}	0.5 (grains – grains) / 1 (grains – walls)
Sample size	$w_{gouge} * L_{gouge}$	1.7 x 20 mm
Particle equivalent diameter	$\phi_{min} - \phi_{max}$	28 – 226 μ m
Number of particles	N	4960
DEM time step	Δ_t	10^{-9} s
Proximity updating period	$\Delta_{t-contact}$	10^{-7} s

3. Simulation results

3.1. Cemented material characterization

The strength of granular materials (may they be cemented or not) and rocks is generally considered to follow the Mohr-Coulomb criterion [(Handin, 1969), (Jaeger, 1971)], which states that the maximum tangential stress τ_{max} that the material can withstand, is the sum of a constant term C (generally called “cohesion”) and an additional term $\tan\varphi$ (generally called “internal friction”) multiplied by the normal stress:

$$\tau_{max} = C + \sigma_n \cdot \tan\varphi \quad (3.1.1)$$

These parameters are not to be confused with the interparticle cohesion (C_{num}) and friction (μ_{num}) that are introduced in the DEM contact laws, since they represent a collective response of the granular material to shearing. To characterize our synthetic cemented gouges, we run independent simulations of biaxial compression of samples identical to those used for our fault gouge (in terms of grain shapes, size distributions, initial solid fraction, interparticle cohesion,

and interparticle friction). Rectangular samples (4 mm wide and 10 mm high) are placed between four rigid walls. The lower wall is fixed in displacement, the upper wall is submitted to a constant downwards velocity V_y , and the lateral walls are submitted to a confining pressure σ_3 , fixed in vertical and rotational motions, and free to move horizontally. For each cementation level and each initial porosity, three tests are performed with confining stresses of 10 MPa, 40 MPa, and 80 MPa. Vertical stress σ_1 is monitored during vertical compression.

Figure 5 provides illustrative results for a numerical cohesion $C_{num} = 1000 \text{ MPa}$ (corresponding to $P_{cem} = 38\%$ in the dense case and $P_{cem} = 40\%$ in the mid-dense case).

Results show that dense samples quickly reach a peak strength before softening towards a plateau value, while mid-dense samples are less stiff and reach the same plateau (approximately at the same level of vertical strain) without passing by a well-defined peak. When plotting the Mohr circles corresponding to the maximum values of σ_1 (Figure 5 – b), we confirm that all samples follow the Mohr-Coulomb plasticity criterion, which makes it possible to characterize their cohesion C and internal friction angle φ . Young's moduli E are also extracted based on the stiffness of the samples at low ($<1\%$) vertical strains.

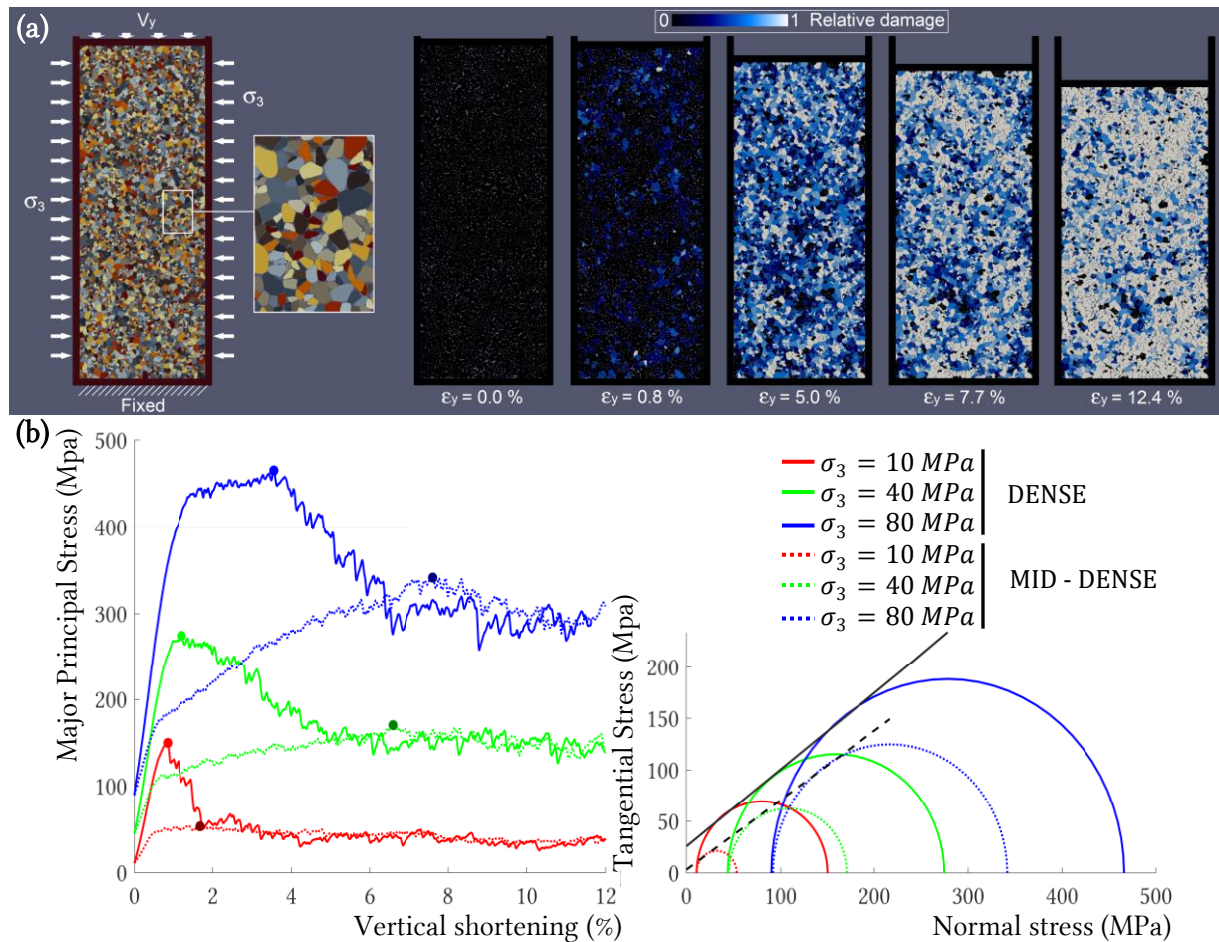


Figure 5. Illustrative results for a numerical cohesion $C_{num} = 1000 \text{ MPa}$ (a) Views of experiment and damage evolution for different percentage of vertical shortening under confining stress of 80 MPa - (b) Major principal stress as a function of vertical shortening and associated Mohr circles, for three confining stresses (10MPa, 40MPa, and 80MPa) for both dense and mid-dense samples.

Similar Mohr-Coulomb graphs were plotted for the other C_{num} values and also result in following the Mohr-Coulomb plasticity criterion. Results are gathered in Figure 6 and show that internal friction φ is only moderately influenced by the cementation level in the mid-dense samples, and is a non-monotonous function of the cementation in the case of dense samples. It is also strongly linked to initial density: mid-dense samples have friction angle values of 32-35°, while dense samples have friction angle values up to 36-44°. Cohesion increases monotonously with cementation (as found in the literature by (Wissa, 1965) and (Lade & Overton, 1989)) and reaches much larger values for dense samples (up to 70 MPa for $P_{cem} \approx 100\%$) than for mid-dense samples (up to 20 MPa). It can also be noted that a certain percentage of cementation is needed to have a measurable cohesion within the gouge ($P_{cem} > 20\%$ for mid-dense samples and $P_{cem} > 10\%$ for dense samples). However, Young's modulus is rather unaffected by cementation and is close to 16-17 GPa for mid-dense samples and to 25-26 GPa for dense samples.

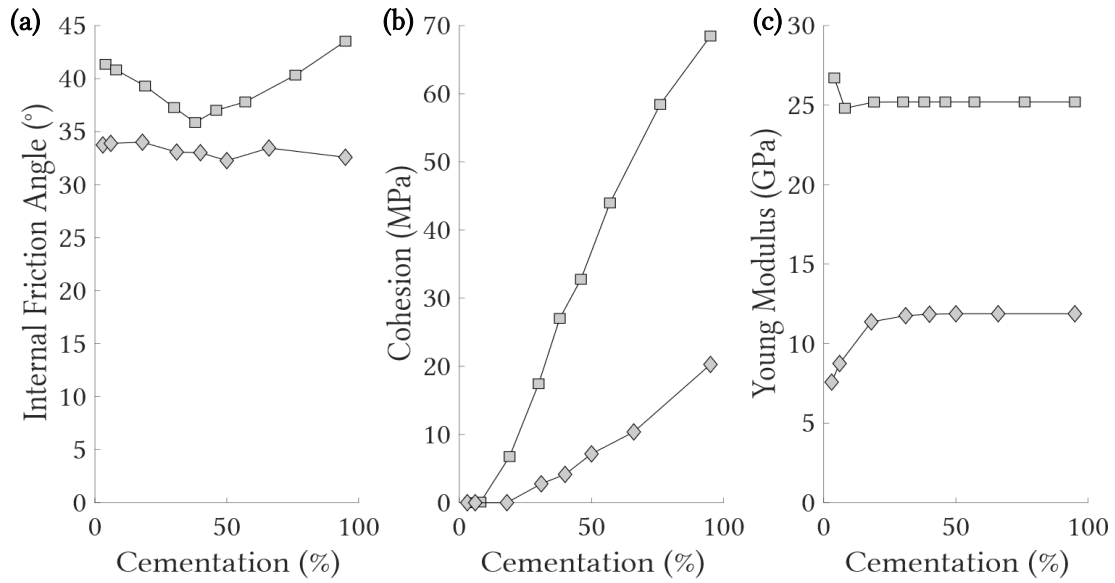


Figure 6. (a) Internal friction angle ($^{\circ}$), (b) Cohesion (MPa) and (c) Young Modulus (GPa) as a function of the Cementation (%) for dense and mid dense samples.

3.2. Influence of the cementation on gouge kinematics

3.2.1. Effective friction and dilation

330 For dense samples, several simulations with various cementation levels are performed. In the next sections, we will use the effective friction $\mu^* = \tau/\sigma_n$ (i.e. total tangential force τ resisting to fault sliding, divided by the applied normal force σ_n) and the dilatancy $\varepsilon_y = dy/w_{gouge}$ (i.e. volume variation dy in the direction of the gouge thickness w_{gouge}) to analyze the mechanical behavior of gouges, as is done in other studies [(GRD Midi, 2004), (Azéma & Radjaï, 2014),
335 (Berger et al., 2015)]. It is important to keep in mind that cementation makes μ^* dependant on the normal load and thus different of a Coulomb-like friction coefficient, hence the term “effective friction”.

(Figure 7 – a & b) provides typical curves of the measured effective friction of the fault as a function of the horizontal displacement imposed to the upper wall. In all cases, the tangential
340 force increases linearly until a maximum effective friction μ_p^* , demonstrating the maximal effort that the loading system must provide to reorganize the gouge and accommodate imposed shearing. The linear elastic part of the curves represents the stiffness of the granular material. It should be noted that this stiffness is only related to the gouge layer itself since no other compliance (related to the surrounding medium, for example) is considered in the simulations.
345 All simulations with initial dense samples follow the same elastic slope, and adding more cementation extends the elastic part before the peak (Figure 7 – b).

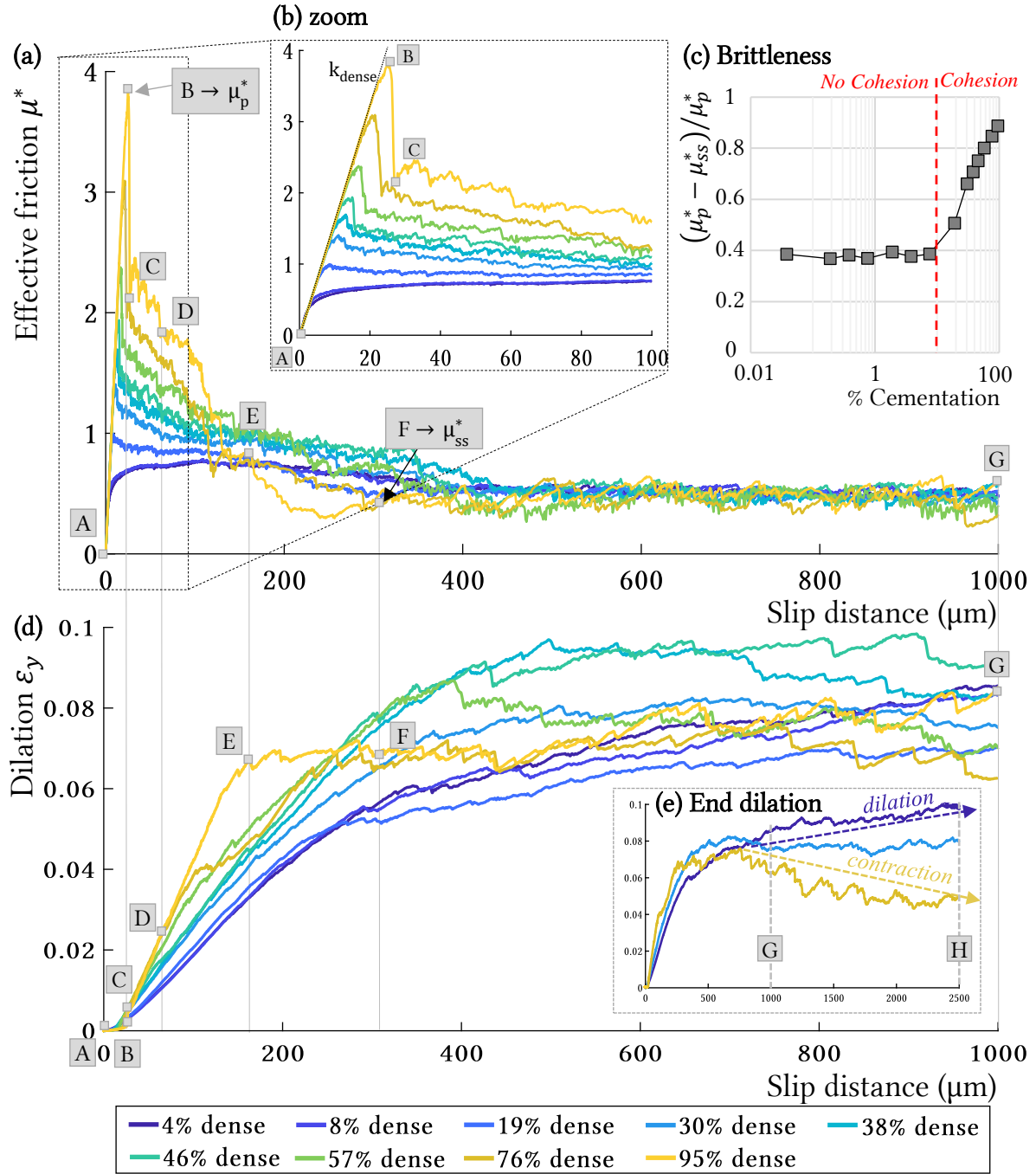


Figure 7. (a) Effective friction curve for different percentage of cementation for dense samples as a function of the slip distance (μm) – (b) Zoom in on the peak – (c) Brittleness as a function of cementation, the brittleness is expressed as the ratio of $(\mu_p^* - \mu_{ss}^*)$ divided by μ_p^* – (d) Dilation variation (μm) as a function of the slip distance (μm) for dense samples – (e) Dilation variation (μm) as a function of the slip distance (μm) for dense samples, higher slip distance. Total simulation from “A” to “H”. Letters correspond to different steps in curves presented: [A] is the initial state before shearing and is identical in all cases. [B] is the peak location, [C] is the end of the first peak (only appears for dense samples with a lot of cementation), [D] is half-peak, [E] is the end of the major dilation phase, [F] is the observed end of the effective friction peak, [G] is a common state for beginning of steady-state and [H] is the end of simulation with $s=2500 \mu\text{m}$ (results table in Supporting Information S7). The case “0 cementation” is not represented here as it is similar to the case with 4% cementation in terms of friction and dilation

variation. It should be noted that these results are not in the range of small deformations, as the total slip displacement ($H=2.5\text{mm}$) is higher than the gouge thickness ($\approx 1.75\text{mm}$).

360 According to the literature, shear strength is enhanced with cohesion, and thus with the increase of cementation (Wissa, 1965), (cf. Figure 6 – b). Depending on the cementation level of each simulation, the peak strength evolves from a smooth, delayed, and of moderate amplitude shape (mildly cemented cases) to a sharp, short, and intense shape (ultra-cemented cases), (Figure 7 – a & b). Cohesive strength in granular materials is known to correlate with an increase in the
365 brittleness of the material (Das et al., 2014). (Figure 7 – c) presents the evolution of brittleness within the sample, indicating the over-consolidation of the material. A qualitative change in behavior is observed close to $P_{cem} = 10\%$. This transition corresponds to the value where cementation starts to induce cohesion within the gouge (red line). From this moment we observe a marked evolution in terms of peak strength, with the emergence of a sharp peak strength
370 increasing with cementation. After the peak, the apparent strength decreases in all cases towards a plateau, which corresponds to a steady-state friction and does not evolve significantly anymore until the end of the simulation. All steady-state values oscillate around the same effective friction μ_{SS}^* , (averaged from the beginning of the plateau until the end of the simulation), very close to 0.5 (ranging from 0.45 to 0.51). It is interesting to notice that this
375 value is in agreement with other numerical studies (Rathbun et al., 2013), but lower than typical 3D experimental values (which are usually above 0.6). This discrepancy is related to the 2D character of the simulations (Frye & Marone, 2003).

For dilation, different behaviors are also observed according to the percentage of cementation within the gouge (Figure 7 – d). For $P_{cem} \leq 10\%$, dilation is similar to a case without
380 cementation as the cohesion in the sense of Mohr-Coulomb is smaller than 1MPa (i.e. negligible compared to the normal stress). A progressive dilation until the steady-state “G” is observed. The increase of cementation (for $P_{cem} \geq 10\%$) seems to accelerate the dilation of the gouge (Figure 7 – d), which appears earlier with slip distance. This dilation enhancement is possible because some frictional contacts begin to form with the breakage of cemented bonds. Observing
385 the second part of simulations from $s=1\text{ mm}$ to $s=2.5\text{ mm}$ (Figure 7 – e), we highlight three main tendencies: materials with medium cementation ($\sim 10\% \leq P_{cem} \leq 75\%$) reach a stabilized density whereas mildly cemented materials continue to dilate and highly cemented materials present a contractive behavior. Mildly cemented materials ($P_{cem} \leq 10\%$) present more frictional contacts than cohesive contacts and frictional particles are known to enhance
390 dilation (Roy & Luding, 2017). For extremely high cementation ($P_{cem} \geq 75\%$), although the

steady-state friction value announces a friction stabilization “G”, a contracting behavior is observed later (from “G” to “H”). This contracting is linked to the dislocation of the asperities formed by cohesive links (i.e. agglomerates) at the beginning of the shear localization “F”, see Section 3.4.

3.2.2. Interface failure modes

Cohesive strength correlating with brittleness increase has a major influence on strain localization (Maurer, 1965). From observations on friction and dilation (for dense samples), our results can be gathered in three different cemented materials: mildly-cemented ($P_{cem} \leq 10\%$), cemented ($10\% \leq P_{cem} \leq 75\%$), and ultra-cemented ($P_{cem} \geq 75\%$), corresponding to three modes of deformation zone. Figures 8, 9, and 10 present the evolution of damage between grains during sliding for three different percentages of cementation, belonging to each of these three classes of materials. The rupture of a cohesive bond is represented by the increase of damage of the concerned grains. This damage is set to 0 for each grain when cohesive bonds are first established (all the bonds are intact) and may evolve until 1 if all these bonds reach the “broken” status (cf. Section 2.2). It is thus a relative damage with respect to an initial state. The representation of the relative damage gives a picture of the state of cementation between grains and their location within the gouge. As shear band formation and evolution varies with the level of bond strength (Jiang et al., 2013), the damage will allow following the formation of failure patterns (Riedel cracks, shear bands, etc.) and their orientation.

- (i) The mildly-cemented material is a medium where inter-particle cohesion introduced between grains is not sufficient to maintain cohesive bonds during shearing. Figure 8 presents the simulation for $P_{cem} = 4\%$, revealing very few tensile forces in accordance with the low percentage of cementation in the sample. As soon as the upper rock wall is set into motion, almost all cohesive bonds break and only a few of them resist until friction peak “B₄”. Dilatancy is found to influence shear bands and strain localization (Mead, 1925), and the limited dilation in the first stages of shearing is consistent with the absence of shear band formation.

Dense - $P_{cem} = 4\%$

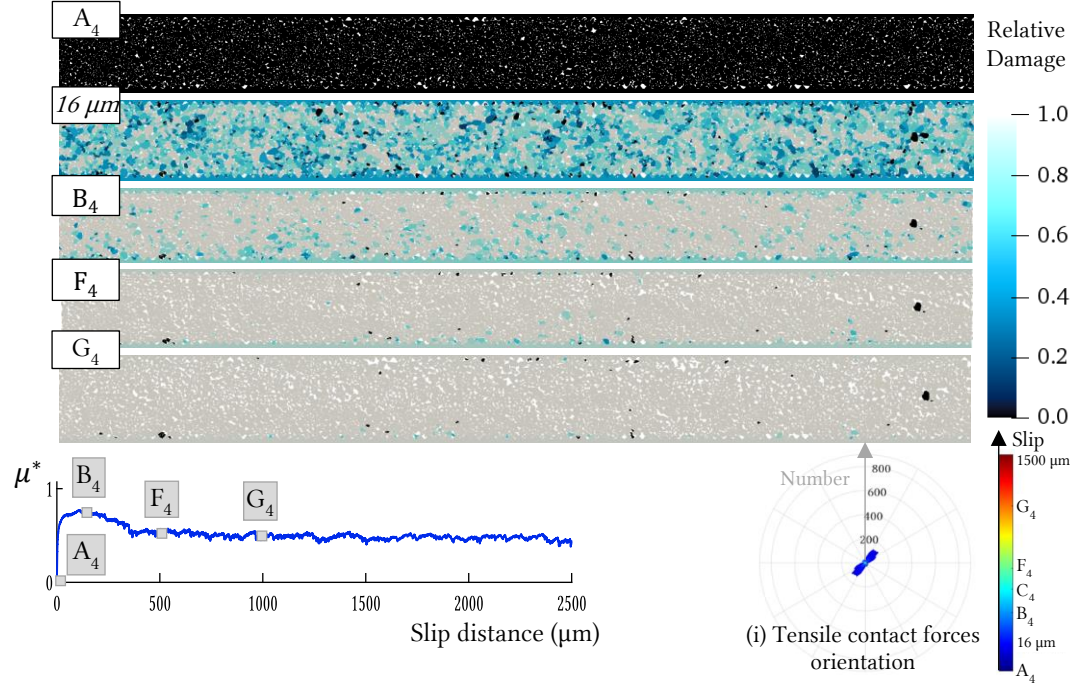


Figure 8. Relative damage snapshot for $P_{cem} = 4\%$ in the dense sample (entire granular gouge). Letters correspond to different steps in the curves presented in Figure 7 (A₄: no damage and no-slip distance, G₄: maximum damage and slip distance of 1mm). (i) Tensile contact force orientations allow getting a grasp on the way load is transferred through a granular sample. This information is coded in a polar diagram which provides the distribution of the orientation of tensile contacts.

(ii) The second type of behavior in Figure 9 corresponds to a cemented granular material ($P_{cem} = 38\%$). In contrast with the first case, this material presents clear augmentation of tensile forces for both initial states “A₃₈” in dark blue and final states in red in (Figure 9 – a & b). Tensile contacts then reduce from effective friction peak “B₃₈” to the end of the peak “F₃₈” with the breakage of cohesive bonds, but many of them remain active, and influence gouge behavior. Friction peak “B₃₈” is the starting point of a movement in the gouge with the highlighting of a preferential localization of cohesive bonds rupture (red arrow in Figure 9 is considered as the first Riedel deformation (Tchalenko, 1970)). This rupture develops in the next stages of the simulation “B₃₈ to H₃₈” with a pattern similar to a Riedel crack R1 (oriented in the sheared direction, $\sim 12^\circ$ from the upper wall). The progression of the Riedel cracks towards a shear band increases until the end of the effective friction peak, where it is no longer detectable among the damage zone. The different Riedel geometries are associated with different shear deformation degrees. R’ shear bands are not visible in the numerical results, but we observe high angle Riedel shear R2 or T (for tensile crack). This is in line with findings reported in

(Cho et al., 2008), who highlighted that tensile fracturing is very important in the development of a shear zone, and particularly at low normal stress. From friction peak “B₃₈”, damage evolution also highlights the presence of cohesive agglomerates formed by intact bonds within the gouge (ex: Ag₁), with size decreasing with time. In contrast to mildly cemented material where contacts take place between two particles, contacts occur here between clusters of cohesive grains. These clusters can lead to rather inhomogeneous behaviors inside the granular gouge, changing the whole geometry and particle size distribution. Similar observations were made by [(Cho et al., 2008) & (Rognon et al., 2008)]. Cohesive agglomerates also participate in increasing the overall dilatancy before steady-state (Figure 7) as found by (Lade & Overton, 1989) for large cemented particles at low confining pressures. Even though dilation is needed to observe shear bands, this cemented material (presenting the highest dilation after peak strength) inhibits the persistence of shear bands until the end of the shearing. This may be due to the important breakage of cohesive links into frictional contacts after the end of effective friction peak.

Dense - $P_{cem} = 38\%$

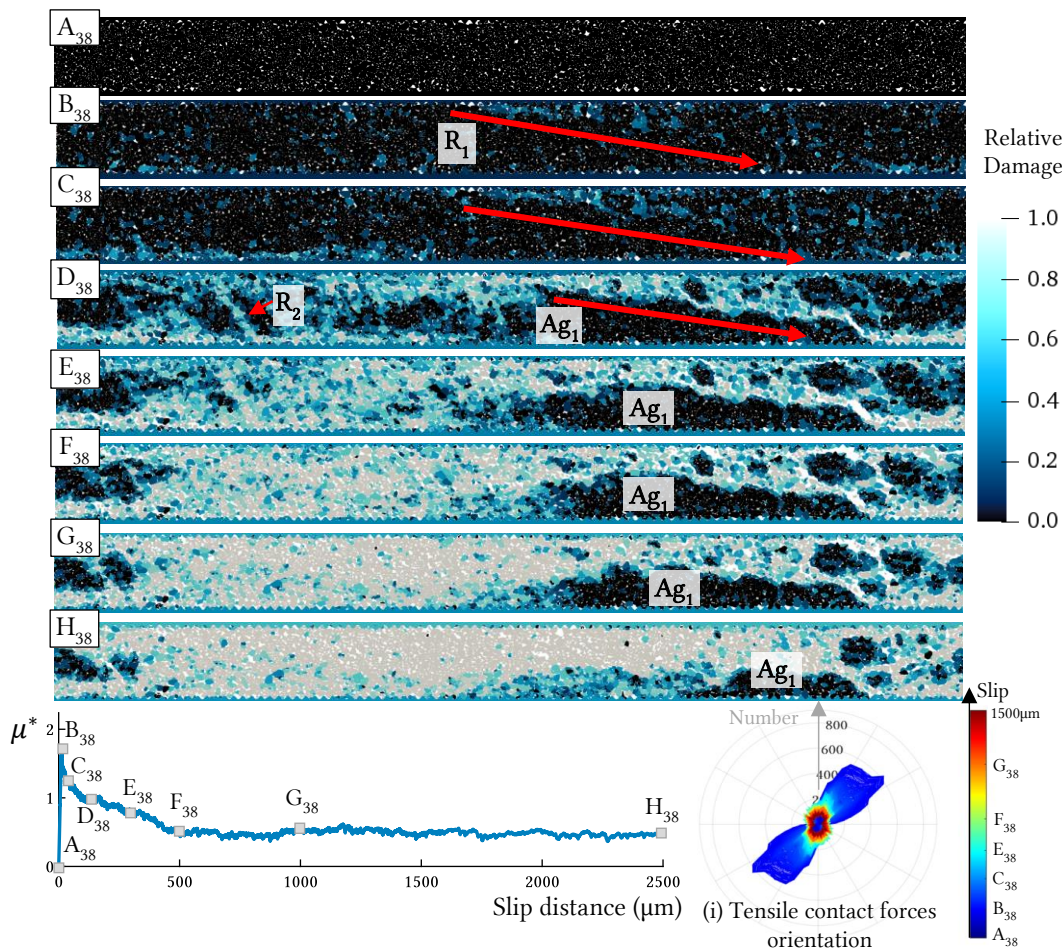


Figure 9. Relative damage snapshot for $P_{cem} = 38\%$ in the dense sample (entire granular gouge). Letters correspond to different steps in the curves presented in (**Figure 7**). (A38: no damage and no slip distance, H38: slip distance of 2.5 mm). “Ag1” denotes a large agglomerate followed during its motion. The red arrow follows the low angle Riedel shear “R1” inside the gouge and “R2” is an example of a high angle Riedel shear band. (i) Tensile contact forces orientation allow getting a grasp on the way load is transferred through a granular sample. This information is coded in a polar diagram which provides the distribution of the orientation of tensile contacts.

(iii) Increasing again P_{cem} leads to an ultra-cemented zone ($P_{cem} = 95\%$) where most cohesive bonds stay intact during the entire simulation (Figure 10). The numbers of tensile forces are obviously higher than in previous materials (Figure 10 – i) and correspond to (Lade & Overton, 1989) results. This highly cemented rock enhances the formation of two Riedel cracks R at the second friction peak in “C₉₅”. Then, “D₉₅” shows the largest Riedel bandwidth, as this step also corresponds to the maximum dilation peak in the simulation. In the next steps, from “E₉₅” to “H₉₅”, Riedel crack widths progressively reduce in favor of a horizontal shear localization S at the top of the granular gouge in “H₉₅”. This shear bandwidth reduction was also observed in other numerical studies with the increase of strain inside the model (Cundall, 1989). As previously supposed (section 3.2.1), the progressive breakage of cohesive agglomerates (i.e. asperities) at the interface between gouge and rock boundary seems to explain the contractive response observed in (Figure 7 - e) from “G₉₅” to “H₉₅”. The shearing localizes on the bottom or top part of the gouge (depending on the simulation) and lets the majority of particles (still cemented) behave as a single solid-like body. This shearing or “active” zone increases with slip distance.

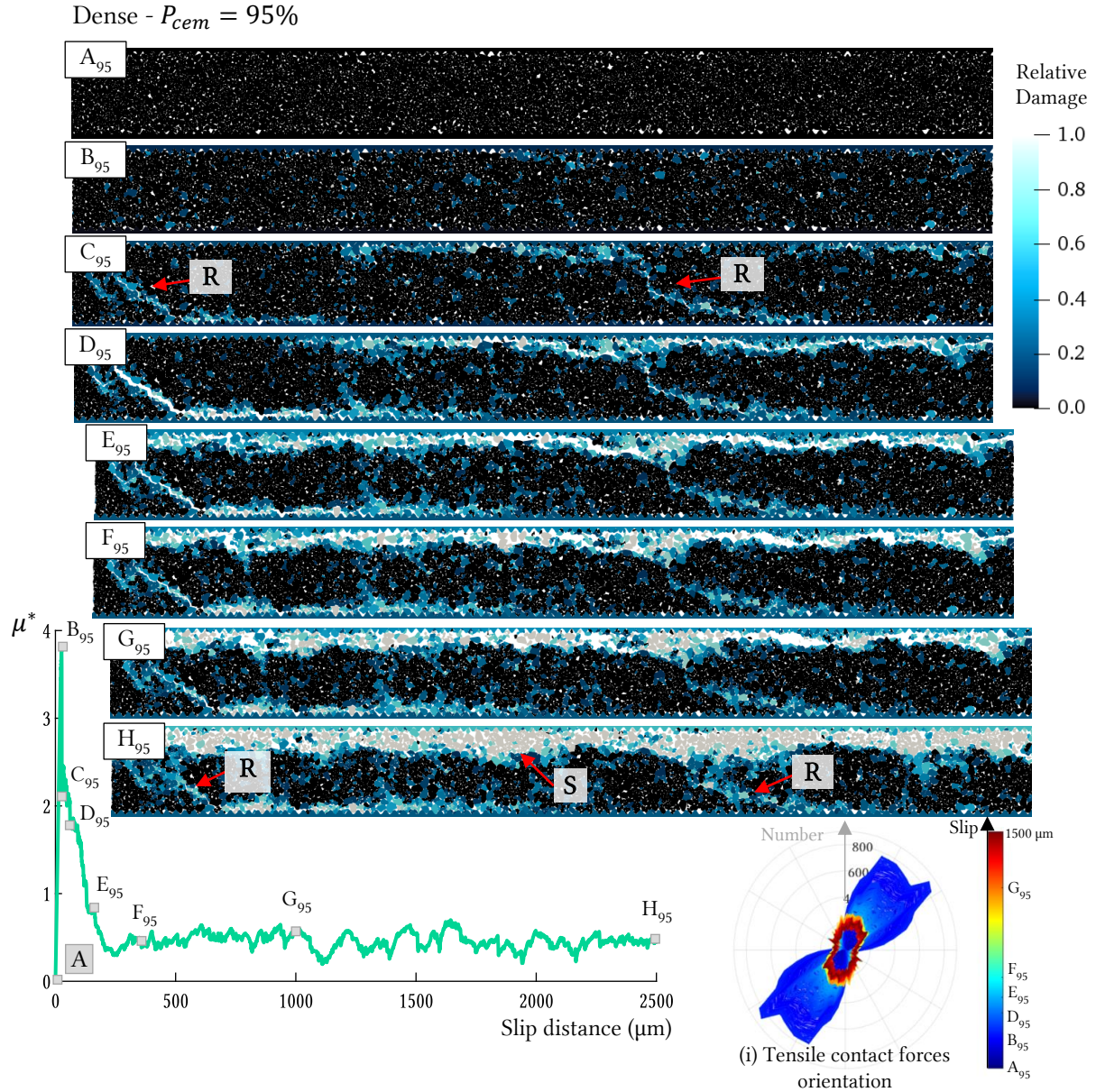


Figure 10. Relative damage snapshot for $P_{cem} = 95\%$ in the dense sample (entire granular gouge). Letters correspond to different steps in the curves presented in (Figure 7). (A95: no damage and no slip distance, H95: slip distance of 2.5 mm). R represents the Riedel shear bands and S the horizontal shear localization. (i) Tensile contact force orientations allow getting a grasp on the way load is transferred through a granular sample. This information is coded in a polar diagram which provides the distribution of the orientation of tensile contacts.

3.3. Influence of initial porosity with cementation

The same percentages of cementation have been tested on a second set of samples with a larger initial porosity $P_{pore} = 16\%$ (termed as mid-dense in what follows, as opposed to the dense samples with $P_{pore} = 11\%$). The three cementation levels previously highlighted have been kept to compare the results between dense and mid-dense samples. The global tendency observed

for mid-dense samples is similar as for dense samples, but we note an influence of both initial
 490 porosity and cementation on the strength of cemented materials.

The increase of initial porosity is supposed to reduce the fracture strength (Taylor, 1948). Our
 results present the same conclusion, but different shapes of effective friction peak are observed:
 the peak strength may be sharp, short, and intense (dense and highly cemented cases) or smooth,
 delayed and of moderate amplitude (mid-dense and moderately cemented cases), (Figure
 495 11Erreur ! Source du renvoi introuvable. – a & b). The denser sample shows higher dilation
 rates than the mid-dense sample (Figure 11 – d), as the initial gouge is initially more compacted
 (Wood, 1990). When the steady-state is reached, maximum dilatancy is also observed for denser
 initial samples with twice the deformation obtained with mid-dense samples, for all initial
 cementations ($\varepsilon_y = 8\%$ for dense samples vs $\varepsilon_y = 4\%$ for mid-dense).

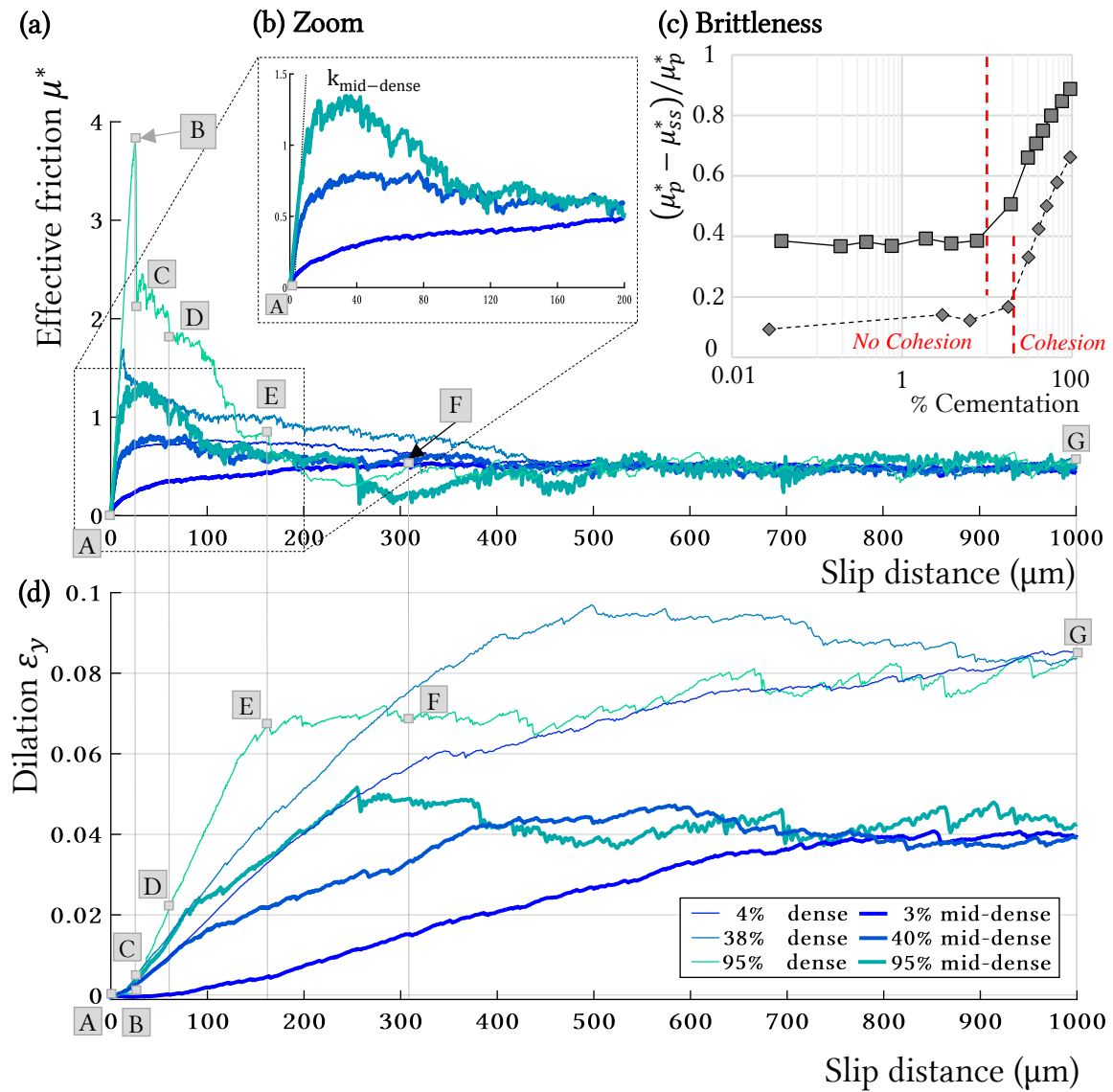
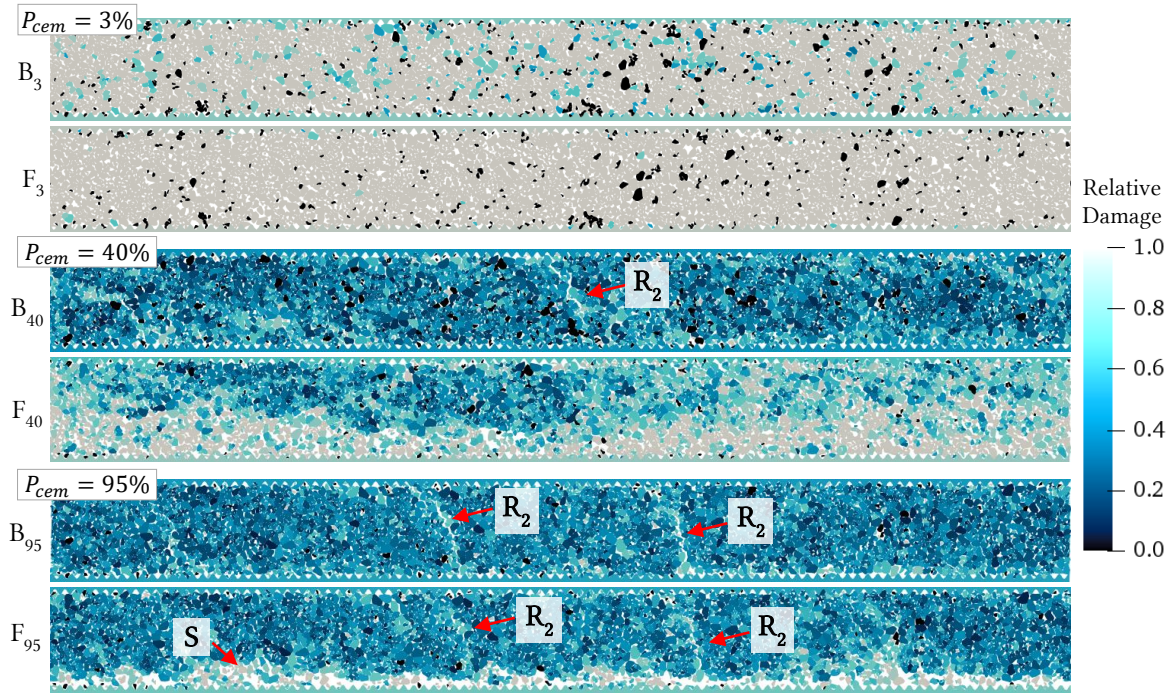


Figure 11. (a) Effective friction curve, comparison between dense and mid-dense samples as a function of the slip distance (μm) for the three different cemented material highlighted – (b) Zoom in on the peak for mid-dense samples – (c) Brittleness as a function of cementation for both porosity states, the brittleness is expressed as the ratio of $(\mu_p^* - \mu_{ss}^*)$ divided by μ_p^* – (d) Dilation variation (μm) as a function of the slip distance (μm) for dense and mid-dense samples. Letters correspond to different steps in curves presented: [A] is the initial state before shearing and is identical in all cases. [B] is the peak location, [C] is the end of the first peak (only appears for dense samples with a lot of cementation), [D] is half-peak, [E] is the end of the major dilation phase, [F] is the observed end of the effective friction peak, [G] is a common state for beginning of steady-state and [H] is the end of the simulation (results table in Supporting Information S7).

(Figure 11 – c) gathers the brittleness based on strength ratio (Bishop, 1971) as a function of cementation for the whole simulation campaign and gives more precise information on the transition zone. We observe that, for samples where a measurable Coulomb cohesion exists, an increase of cementation increases the brittleness of the sample (Figure 11 – c) for both dense and mid-dense samples, and thus leads to enhance the strength of the gouge (Figure 11 – a). However, the increase of initial porosity leads to a weaker material in terms of cohesive strength. Without the effect of cementation, we can observe that the brittleness is almost four times higher for dense samples (i.e. ~ 0.4) than for mid-dense samples (i.e. ~ 0.1). The mid-dense case with the lower cementation is assumed to be here the weaker material tested. When the cementation level reaches values close to its maximum ($P_{cem} \approx 100\%$), then the brittleness can reach almost 0.9 in the dense material and almost 0.66 in the mid-dense material. It is very likely that such high values are related to the fact that the cementation of the sample is very high while the confining stress (40 MPa) is rather low (Lade & Overton, 1989).

Mid-dense samples also present higher relative damage with easier grains reorganizations (Figure 12), which agrees with the relatively low Coulomb cohesion involved. One high angle Riedel shear band R2 in the 40% case, and two high angle Riedel cracks R2 in the 95%, are followed by a horizontal shear localization S at the bottom of the granular gouge. Riedel bands observed do not have the same orientation as those observed with dense materials and are less persistent during shearing. The more ductile character obtained for mid-dense samples could be a reason for the different Riedel angle observed (Misra et al., 2009). The non-persistence of shear bands for mid-dense samples is in adequation with previous studies on sandstones [(Dunn et al., 1973) & (Antonellini & Pollard, 1995)]. They have shown that gouges with high porosities enhance a distributed deformation that takes the form of cataclastic flow, in contrast with low porosity sandstones which better fails by localization and strain softening (Hirth & Tullis, 1989).

(a) Relative damage - Mid-dense



(b) Tensile contact forces orientation

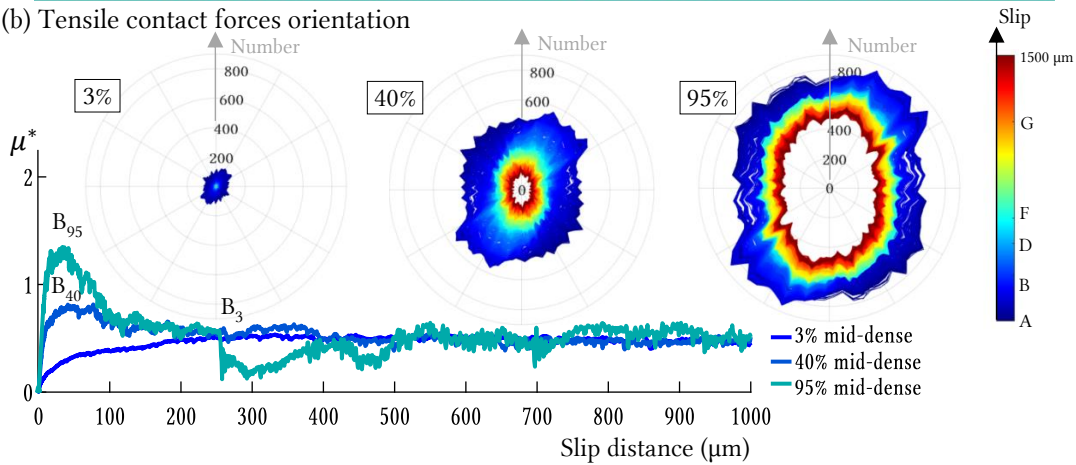


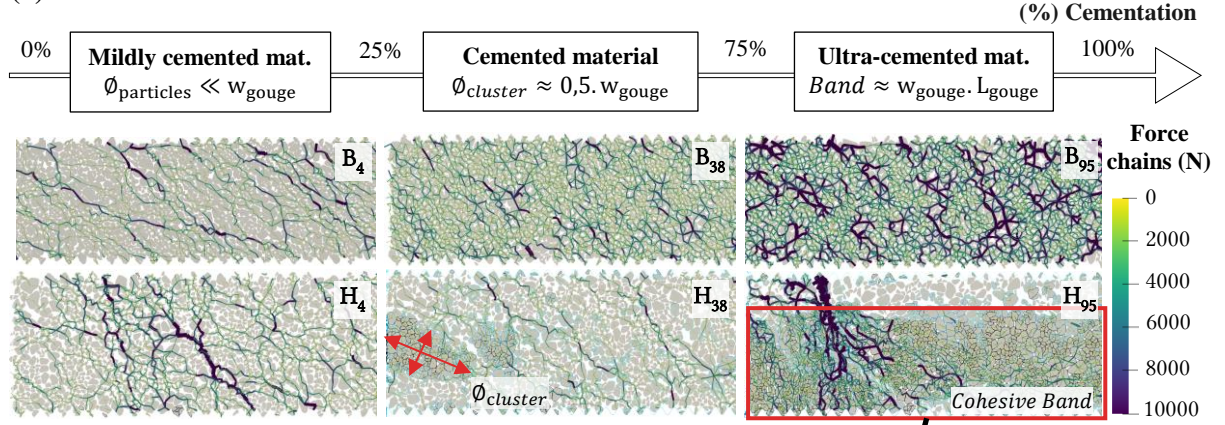
Figure 12. (a) Relative damage snapshots for mid-dense sample (entire granular gouge). For both peak [B] and end [F] of effective friction peak. Letters correspond to different steps in the curves presented in Figure 7. R2 represents high angle Riedel shear bands and S the horizontal shear localization. Evolution of ductility with cementation and porosity - (b) Tensile contact forces orientation allows to get a grasp on the way load is transferred through a granular sample. This information is coded in a polar diagram which provides the distribution of the orientation of tensile contacts.

3.4. Influence of ductility with cementation and porosity

Force chains are key elements to understand the kinematics of the gouge layer and illustrate changes in ductility behavior inside the granular gouge as a function of cementation or porosity. It should be noted that, in the present context, “ductility” is to be understood in the sense of granular mechanics: it is related to the suddenness or slowness of the post-peak frictional weakening but does not involve any visco-plastic phenomenon.

Evolution of ductility with cementation - Commonly used in granular physics [(Majmudar & Behringer, 2005), (Zhang et al., 2017)] for load transfer observation, force chains are plotted
550 between grains centers (for each contact). The norm of the contact force is coded by the
thickness and color of each chain. It allows to get a grasp on the way load is transferred through
a granular sample. The same information can be coded in polar diagrams which provide the
distribution of the orientation of contact normal vectors. The mildly cemented materials
($P_{cem} < 10 - 25\%$) show a ductile behavior, with a progressive particle reorganization, and no
555 localized shear is observed in (Figure 8). It displays a preferential orientation for force chains
inclined at 45° from the upper rock wall (Figure 13 – a). Similar orientations of force chains
have been observed by (Morgan & Boettcher, 1999) for circular particles. The change of
orientation of normal forces at 45° appears before the effective friction peak, showing that the
gouge started to dilate before reaching the peak. The evolution of the granular flow gives way
560 to simple contact law with inter-particle friction only. Once the gouge has dilated, grains can
reorganize to allow shearing, and the gouge tends towards a stationary state of sliding from the
end of the effective friction peak to the end of the simulation. The combination of limited
cementation (mostly frictional contact, no cohesion in the sense of Mohr-Coulomb), gouge
dilation (Figure 7), and preferred orientation of force chains seem to confirm a typical granular
565 Couette flow for the mildly cemented zone [(GRD Midi, 2004) & (Da Cruz et al., 2005)].

(a) Force chains evolution



(b) Zoom in on the 95% cementation

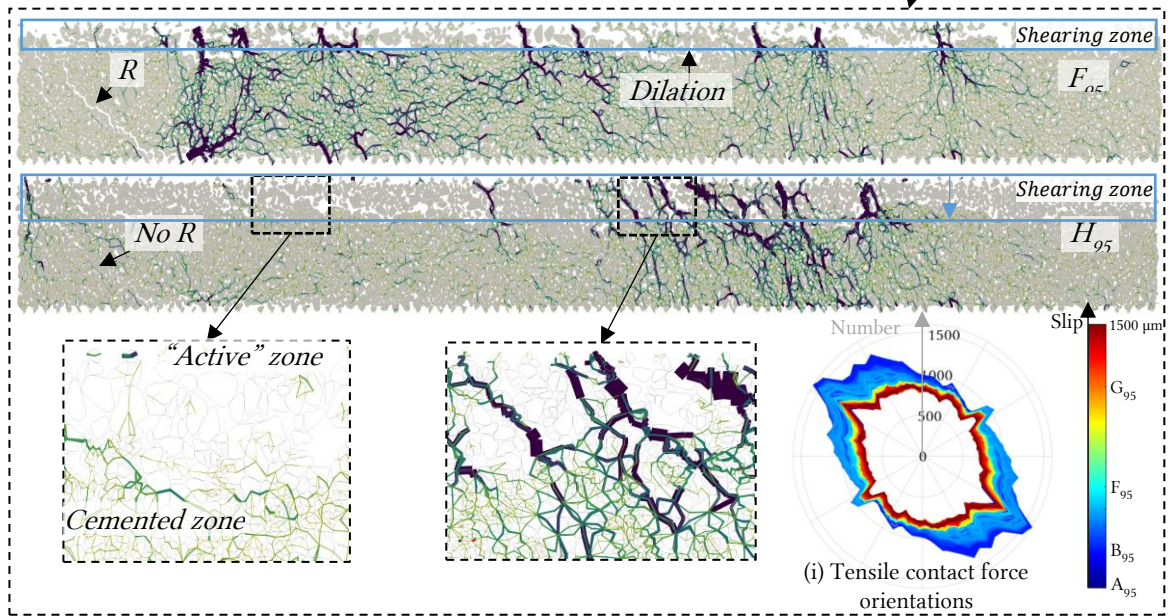


Figure 13. (a) Snapshot of the force-chains network for dense samples at friction peak [B] and at the end of simulation [H] (from 0 to 10^4 N). Force chains are defined according to the typical level of stress present in the system (here the applied normal stress) and thickness evaluates between 0 and 1 between the minimum and maximum strength (0 to $1e4$ N). A cut-off is made at $1e4$ N to have the same visualization for all cases (higher force chains are observed for a high percentage of cementation). – (b) Zoom in on the material with $P_{cem} = 95\%$, snapshot of the force-chains network at the end of friction peak [F] and the end of the simulation [H] (from 0 to 10^4 N) – (i) Tensile contact forces orientation allows getting a grasp on the way load is transferred through a granular sample. This information is coded in a polar diagram which provides the distribution of the orientation of tensile contacts.

With the increase of cementation ($P_{cem} = 38\%$), the orientation at 45° is not yet present at friction peak B, because no significant motion has occurred yet and grains are still in their initial configuration. Instead, there are a large number of smaller ramified force chains distributed in a homogenous distribution of force network. The strength of the material is linked to the development of force chains (Zhang et al., 2017), and our results confirm that the intensity of

force chains is enhanced with cementation, as strength is also enhanced (Figure 13 – a). Combining force chains and relative damage makes it possible to identify from the force network the cemented agglomerates highlighted in section 3.2.2 (red arrows). Each cemented particle is crossed by a force chain, while isolated frictional particles are not (Figure 13 – a).
585 These cemented clusters also modify the particle size distribution within the gouge, which is well-known to act on shear bands formation in addition to the initial density of the sample (Marone & Scholz, 1989).

(Figure 13 – a & b) displays a dense sample with 95% cementation at the end of friction peak. Some particles are detached from the cohesive band and operate alone (within the active or
590 shearing zone), defining clear geometrical asperities. These asperities create contacts between the cemented layer and the rock wall, which concentrate the normal load. A steady-state is reached when enough of this tribological third body has been released to avoid any asperity contact and to produce a three-body sliding (the third body being here the gouge material within the shearing contact zone, more information on third body concept are available in [(Jordanoff
595 et al., 2005) & (Fillot et al., 2007)]). Gouge first dilates thanks to the emergence of asperities (i.e. grains emerging from cohesive bond breakage) and clusters of grains, forming inter-particle bridges, which releases gouge in the interface as the rupture is going on. Normal forces orientation follows the same trend as the dilatancy: a first increase at the first step (due to inter-particle bridge formation) and a come back to the initial state, as the majority of cohesive bonds
600 are still active (Figure 13 – i). Cementation here also enhances local dilation during the strength weakening, increasing local porosity inside the gouge as found by (Faqih et al., 2006).

Evolution of force chains with initial porosity – Figure 14 compares force chains and normal contact orientation for dense and mid-dense samples. Whatever the cementation level, the initial preferred orientation of normal forces at zero displacement (step A) changes between dense and
605 mid-dense samples (Figure 14 – b). Dense samples lead to a homogeneous repartition of contact normal orientations and mid-dense samples present normal forces mostly oriented perpendicularly to rock walls. The evolution between the three cemented materials at effective friction peak is similar for both values of porosity, but denser samples favor a more homogenous distribution of the force network (i.e. force chains (Figure 14 – a)) passing through almost all
610 particles (consistent with previous section showing that the strength increased with a high cemented and dense sample).

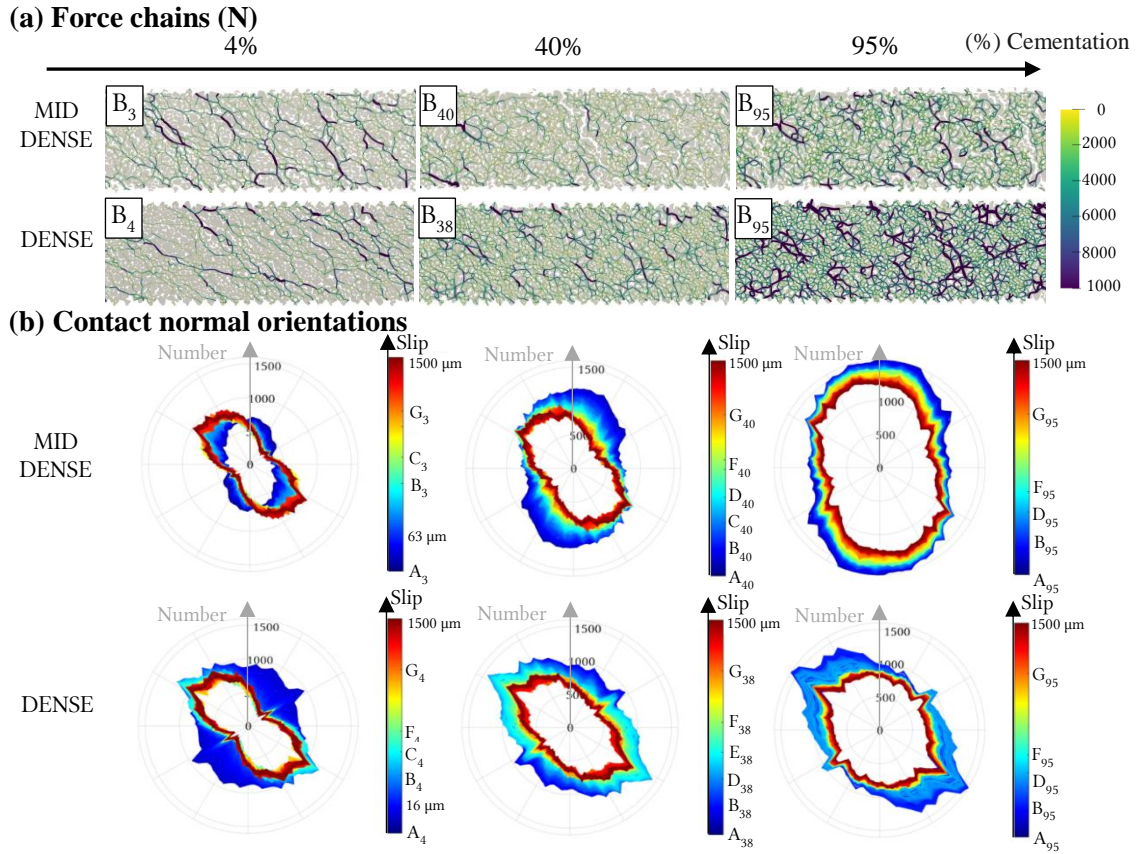


Figure 14. (a) Snapshots of the force-chains networks at the effective friction peaks [B] for six chosen cases (0 to 1e4 N). For 3-4, 40-38, and 95% of cementation. In the pictures, only a quarter of the total gouge is displayed, and even if the global behavior is similar to one quarter, force chains are not homogeneously distributed within the gouge after friction peak. – (b) The graph provides the numbers of contacts with a normal vector oriented in a given direction (using polar diagrams where the Theta-axis is the orientation and the R-axis is the number of contacts), and with a color evolving during the different stages of each simulation.

4. Discussion: a link between gouge rheology and fault zone structure

4.1. Shear bands and weakening mechanisms

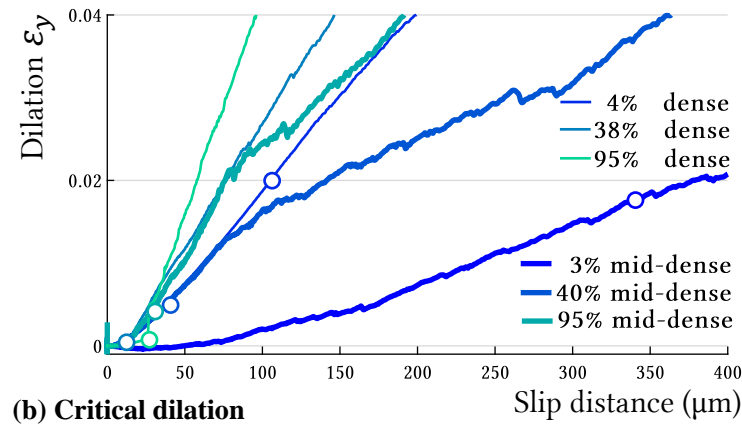
Shear bands and critical dilatancy – Critical dilation can be defined as the necessary dilation for macroscopic shear failure formation (Kranz & Scholz, 1977). In our simulations, it corresponds to the dilation ε_{yp} obtained at the effective friction peak (Figure 15) which is different from the total dilation ε_y previously presented.

- For cases with limited cementation ($P_{cem} < 10\%_{dense} - 25\%_{middense}$) - where 100% frictional contact is quickly reached and no localized shear is observed - the critical dilation is similar for both dense and mid-dense samples and presents the highest values (~ 2% in Figure 15). A high dilatancy rate is present in the pre-peak phase and explains

the important dilatancy observed at friction peak. Porosity alone (without cementation effect) does not have a major influence on critical dilatancy.

- For cases with moderate to high cementation ($P_{cem} > 10\%_{dense} - 25\%_{middense}$), two main trends are observed with the increase of cementation: 1) a decrease of the critical dilation for mid-dense samples, 2) an enhancement of the critical dilation for dense samples. It can be noted that all critical dilations observed in this zone are smaller than in the rectangle “i”. In cohesionless materials, dilation is supposed to be larger for a denser granular gouge, but the introduction of cementation creates the opposite effect. Similar results have been found for other dense cohesive materials through other types of experiments (Faqih et al., 2006). The critical dilation is here smaller for dense samples than for mid-dense samples, a result that may be due to the real cohesion values involved within the sample (i.e. higher for dense sample).
- Comparing shear band formation and critical dilatancy, we can deduce that with more than 1% of critical dilatancy (for both dense and mid-dense samples), shear band formation is inhibited. Then, shear bands persistence until steady-state depends mostly on cementation, and occurs for ultra-cemented materials, corresponding to a critical dilatancy between 0.08 % and 1% (rectangle “iii”). (Noel et al., 2021) found that for Tavel limestone (11% initial porosity corresponding to our dense sample), a critical dilatancy of about 1% has to be reached to obtain shear failure of an initially ductile rock subjected to a pore fluid pressure increase. Their higher critical dilatancy could be explained by the fact that they study intact rocks, but also by the higher confining pressure used and the presence of fluid.

(a) Dilation as a function of slip distance – Zoomed from Fig. 11



(b) Critical dilation

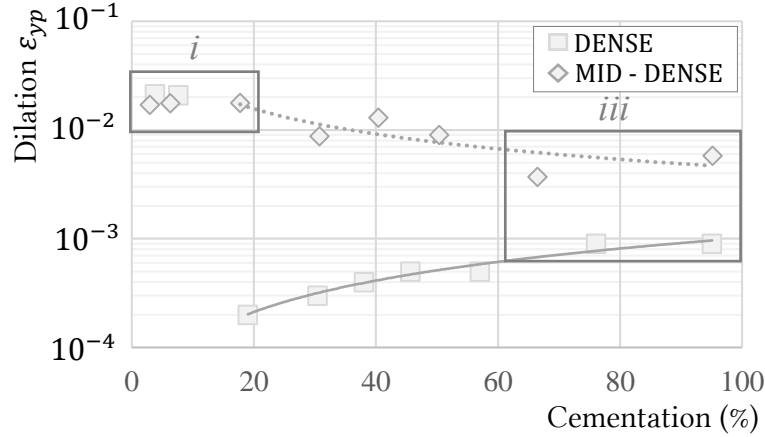


Figure 15. (a) Total dilatancy as un function of slip distance, the marked point locates the critical dilation for the 3 cemented materials (b) Critical dilation for macroscopic failure for both dense and mid-dense samples as a function of the percentage of cementation.

Evolution of weakening mechanisms – In Figure 16, peak length D_{pp} (analogous to the D_c used in rate and state laws), is the distance between the peak of effective friction and the beginning of the steady-state. D_{pp} value is relevant for rupture energy calculation and can be related to the energy needed to weaken the fault until the steady-state of sliding

- (Figure 16 – c) highlights two main trends for D_{pp} : (i) with $P_{cem} < 10\%_{dense} - 25\%_{middense}$, mid-dense samples need a higher displacement than dense samples to reach their steady-state regime (810 vs 300 μm), (ii) with $P_{cem} > 10\%_{dense} - 25\%_{middense}$, D_{pp} decreases with P_{cem} , similarly for both dense and mid-dense samples. Initial porosity seems to affect the peak duration, but only for cases with limited cementation. When cementation is large enough, the initial state of porosity doesn't have an additional influence on D_{pp} . The transition between the two zones corresponds to the mechanical limit between the cohesionless and cohesive model (i.e. formation of

cohesion in the sense of Mohr-Coulomb theory) represented by the red line on graphs. Adding more cementation within the gouge seems to diminish the porosity effect regarding the peak length. The evolution of the peak distance D_p (i.e. distance reached at effective friction peak), is similar to the evolution of critical dilation (Figure 16 – b), and increasing the cementation also tends to balance the change in porosity, leading to a similar peak location.

- Double weakening shapes are observed in some effective friction curves in Figure 16. This pattern seems to be a characteristic of dense cohesive material as our mid-dense case only has one weakening phase. When it exists, the first weakening period seems to follow a linear law and appears for dense samples with $P_{cem} \geq 10\%$. Isolating contributions from each mechanism (bond breakage, dilation, friction), it appears that this first weakening period is mainly due to a mixture between important friction and cement breakage, generating high frictional contacts between the few grains which are not cohesive anymore. The second weakening period obtained for dense cemented material (and corresponding to a simple weakening for mid-dense material), is mainly due to dilation mechanisms. This separation in two phases adds a new key of understanding for weakening mechanisms, especially the first peak which is not due to dilation. Similar double weakening has been observed experimentally as reported in an incoming paper from (Paglialunga et al., 2021).

The weakening zone usually appears with the formation of B and R shears (Mair & Marone, 1999). However, with the separation into two weakening phases, it appears that Riedel bands only form at the beginning of the 2nd weakening phase (letter C in previous figures). In fact, the first weakening phase just allows movement within the gouge by breaking some isolated bonds, but actual sliding needs dilation to operate and thus is only observed within the 2nd weakening.

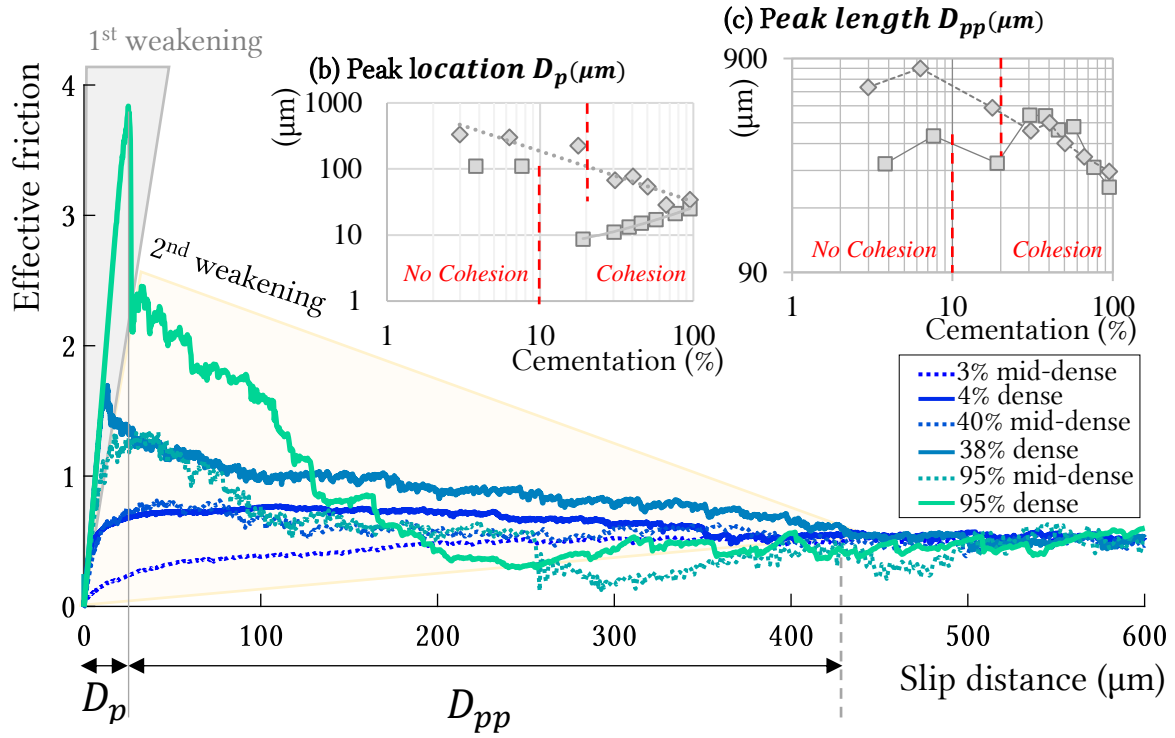


Figure 16. (a) Effective friction curves (b) Peak distance D_p (μm), (c) Peak length D_{pp} (μm), for both dense and mid-dense samples, as a function of the percentage of cementation within the gouge.

4.2. Cemented materials and Mohr-Coulomb theory

4.2.1. Comparison to real cemented material and rocks

The cementation considered in this paper has a clear definition from a numerical point of view but is difficult to characterize on real samples. For this reason, it is instructive to consider instead the Mohr-Coulomb properties of the cemented gouges, for which characterization techniques are available. Figure 17 compares the different synthetic materials tested in this paper (with different percentages of cementation and porosities) with typical rock properties found in the literature (Schellart, 2000), in terms of internal friction angle and cohesion. We observe that our samples have adequate values of internal friction angle (especially in the mid-dense case) and are in the lower range of cohesions. The low cohesion is consistent with the fact that we are simulating cemented gouges instead of intact rock.

Figure 17 let us observed some materials with the same characteristics of cohesion and friction angle: (a) Quartz sand with mildly cemented dense samples, (b) rock “8” (Tennessee sandstone) with 75% cemented gouge (dense), (c) rock “1” (Granite) with highly cemented gouge (mid-dense). Even if some friction angle and cohesion are close to some Mohr-Coulomb values, the resulting strain observed with direct shear on a gouge layer was found to be not consistent with

710 strain from a Coulomb material (Byerlee & Savage, 1992). A fault gouge develops a complex Riedel band structure reflecting a heterogeneous stress field different from intact rocks (Lockner & Beeler, 2002).

Future work might be undertaken to target the Mohr-Coulomb properties of a cohesive rock for which direct shear experimental results are available, in order to propose a direct comparison
715 with our simulations.

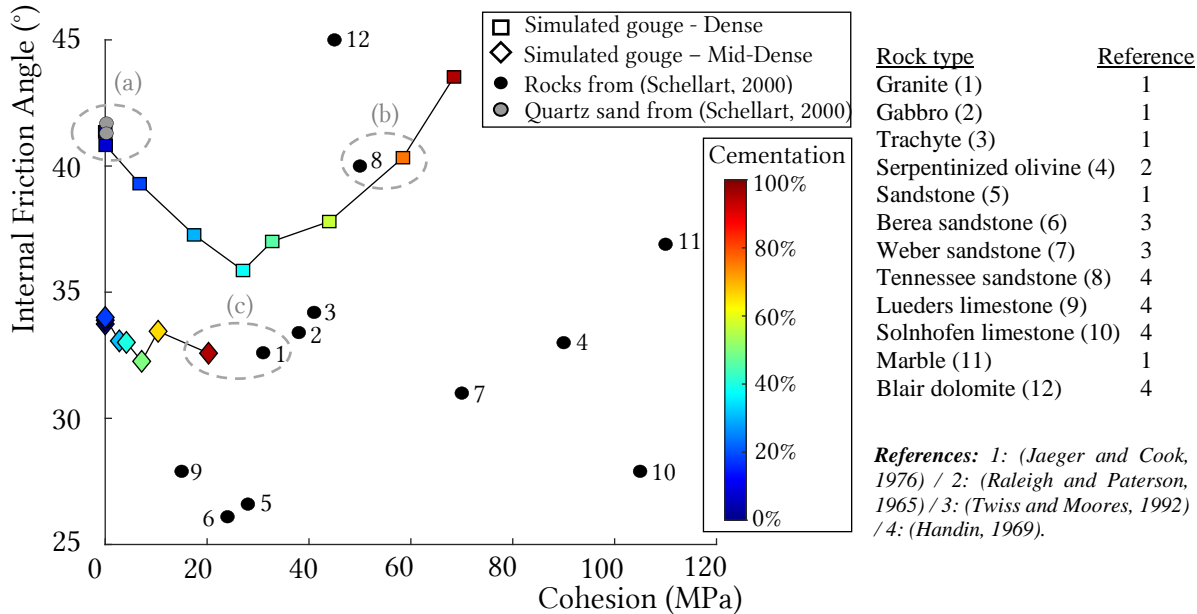


Figure 17. Internal friction angle as a function of Mohr-Coulomb cohesion for the different materials tested for the different percentages of cementation and the two initial porosities (i.e. initial dense and mid-dense samples). Dense samples are marked by squares and mid-dense samples by diamonds. The discs represent Mohr-Coulomb cohesion of different rocks referenced in (Schellart, 2000) listed in the table next to the graph.
720

4.2.2. Discussion about Mohr-Coulomb theory

Cemented gouges have interesting behavior because they are not intact rock and neither simple frictional gouges. In this section, we compare failure criteria applied to intact rock or fault gouge layer to the cemented gouges presented in the study in order to see which criterion can
725 best fit the failure of cemented gouges.

As Mohr-Coulomb theory [(Handin, 1969) & (Jaeger, 1971)] predicts a typical Coulomb failure for intact rocks, (Byerlee & Savage, 1992) also analyzed a fault gouge layer under shearing and observed that it behaves as a Coulomb material, with an elastic deformation until failure. However, (Marone et al., 1992) proposed another adapted criterion that is more suitable to thin
730 fault gouge layer. The two failure criteria considered to support these assumptions are:

$$\tau/\sigma_N = C/\sigma_N + \tan\varphi \quad (4.2.1)$$

$$\tau/\sigma_N = C * \cos \Phi / \sigma_N + \sin \Phi \quad (4.2.2)$$

The first criterion applies to intact rock and the normal and tangential stresses σ_N and τ apply on a shear crack with a clear orientation. It is called “Coulomb failure” and provides the “true” Mohr-Coulomb properties C and φ of the intact rock. The second criterion applies to a domain where shearing occurs in a distributed and continuous way and the stresses σ_N and τ are not requested to apply on a specific crack. Rather, their orientation is related to that of the principal stresses that develop in the sheared domain. This is known as “Coulomb plasticity”. As explained in (Marone, 1995), the first criterion could be applied to faults with very thin layers of gouge, while the second one might be relevant to the case of thick layers of granular gouge where such rotation of the principal stresses could occur. In that case, Coulomb plasticity could lead to a reduction of the effective friction of the fault. This assumption was validated experimentally in a cohesionless case in (Marone, 1995).

Figure 18 presents the effective friction as measured with direct shear experiments as a function of effective friction as predicted by both failure criteria (with both equations 4.2.1 and 4.2.2). With this graph, we can directly compare the peak of strength ratio obtained with both models (direct shear and biaxial test) realized with the same conditions and characteristics (cf. section 3.1). Indeed, gouge behaving as granular material (i.e. with no cohesion) present lower friction than for intact rock as predicted by literature (points under the dotted line). However, cemented gouges present the opposite behavior once the percentage of cementation account for a small cohesion (i.e. for more than $10\% < P_{cem}$ for dense samples and $25\% < P_{cem}$ for mid-dense samples). The increase of cementation increases the effective friction of the cemented gouge compared to intact rock, and the reduction of porosity overstate the difference. It appears that the proposed adapted law 4.2.2 for fault gouges (Marone et al., 1992), does not fit very well with cemented gouges either. The initial stress ratio from the Coulomb criterion (equation 4.2.1) is closer to values found for our cemented gouges but is not suitable as cementation increases.

We hypothesize that one of the reasons that could explain these differences could be the different boundary conditions used for the two kinds of tests (direct shear/ biaxial experiment). Another key of understanding could be the different stress fields present in both models. As we

need further analyses and simulations to confirm these hypotheses, we shall discuss these propositions in a future work comparing different gouges with cement or matrix.

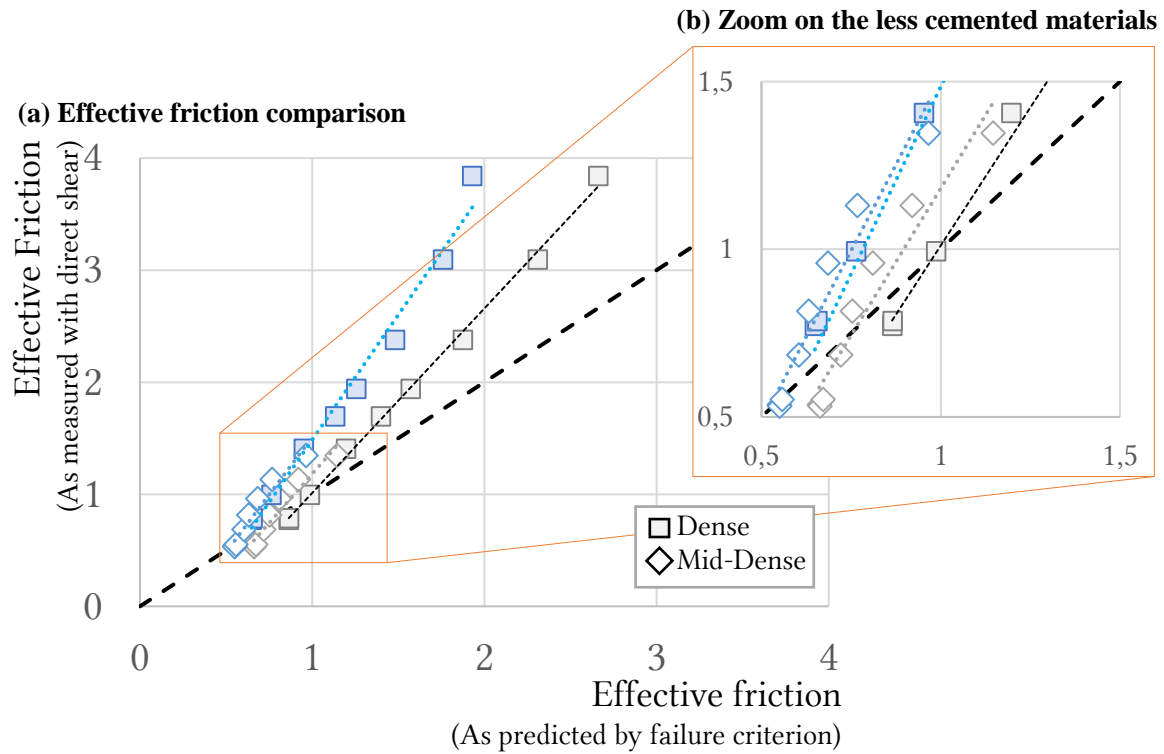


Figure 18. Effective friction as measured with direct shear experiments (simulation campaign) as a function of effective friction as predicted by failure criterion (calculated with internal friction angle and cohesion found with Biaxial tests), for dense and mid-dense samples. The blue line represents the effective friction given for sheared gouge with equation 4.2.2 (Marone et al., 1992) compared to the grey line, effective friction for intact rock with equation 4.2.1 (Handin, 1969).

5. Conclusion

A 2D granular fault gouge model has been implemented in the framework of DEM in order to establish a link between gouge properties (cement and initial porosity) and rheological behavior. One originality of this paper is the use of the angular and faceted shape of particles instead of circular ones. Our results confirm that both initial porosity and cementation influence gouge behavior. They play a role in the internal structure and geometry of the gouge and thus modify the rheological behavior of the fault. In the range of our numerical experiments (normal stress 40 MPa & slip rate 1m/s), the increase of cementation within the gouge leads to an increase of effective strength whereas an increase of initial porosity tends to a reduced strength.

- (i) The peak strength is sharp, short, and intense for dense and highly cemented materials and smooth, delayed and of moderate amplitude for mid-dense and moderately cemented materials. Brittleness is enhanced with cementation, especially in the case of

dense materials. It evolves similarly with the internal cohesion within the gouge and leads to different failure patterns. The ultra-cemented material with low initial porosity presents clear Riedel band formation evolving as in the theory of (Tchalenko, 1970). The high cohesion and internal friction angle values make this material very close to intact rock properties. In opposition, the weakest material is obtained with the highest porosity state and for no cementation: no failure pattern is observed and a typical granular Couette flow is highlighted.

- (ii) Shear failures need a critical dilatancy to form. For mildly-cemented material, not presenting enough cohesion (i.e. $C < 1\text{MPa}$ for mildly cemented material), the same critical dilatancy is observed for both dense and mid-dense samples. The initial porosity does not have a major influence on critical dilatancy for cohesionless materials. However, when cohesion is present within the particles, the critical dilatancy appears to be smaller for denser samples and increases with cementation, whereas mid-dense samples present the opposite behavior.
- (iii) Effective friction curves present double weakening shapes for dense samples with enough cementation (i.e. presence of cohesion). The first weakening phase is triggered by the rupture of cohesive bonds and friction, whereas the 2nd weakening comes with the dilation peak. The peak length (analogous to the D_c from rate and state laws) mainly decreases with the percentage of cementation.
- (iv) The increase of cementation increases the effective friction of the cemented gouge compared to intact rock, especially with dense cemented gouges. Effective friction from the Coulomb failure criterion or the Coulomb plasticity criterion (Marone et al., 1992) do not predict very well our values for cemented fault gouges. The different boundary conditions and stress fields obtained for the direct shear experiment and the biaxial test could explain the difference, but further analyses are needed to confirm these hypotheses.

In future work, we will extend this numerical campaign to cover a wider range of normal stresses and gouge thickness, in order to derive an empirical slip-weakening friction law based on the micromechanical properties of the gouge. This law could then be implemented in dynamic rupture modeling at a higher scale for a dialog with seismological data. Depending on the model, contact laws, and phenomena studied, other contributions could be added to the friction decomposition proposed.

Acknowledgments and Data Availability Statement

We thank Arnold Blaisonneau, Julie Maury, and Theophile Guillon from BRGM (France) for fruitful discussions all along with the research. We also thank François Passelègue for his kind remarks and discussions at the end of the paper. And we also express gratitude to the reviewing team for the interesting and instructive comments on the first paper version. This study was funded by INSA de Lyon, a ministerial grant led by A. Daouadji. The authors declare that they have no competing financial interests. Numerical data and software used for this research are available in these in-text data citation references: Casas et al. (2020), “Cohesion and Initial Porosity of Granular Fault Gouges”, Mendeley Data, V2, doi: 10.17632/7c3dcj7spw.2 (<http://dx.doi.org/10.17632/7c3dcj7spw.2>). Other explanations are included in this paper and its supporting information file or available by contacting the corresponding author at nathalie.casas@insa-lyon.fr (Nathalie Casas).

References

- An, L.-J., & Sammis, C. (1994). Particle Size Distribution of Cataclastic Fault Materials from Southern California : a 3D study. *Pure and Applied Geophysics*, 143(1), 203–227.
<https://doi.org/10.1007/BF00874329>
- Anthony, J. L., & Marone, C. (2005). Influence of particle characteristics on granular friction. *Journal of Geophysical Research: Solid Earth*, 110(8), 1–14. <https://doi.org/10.1029/2004JB003399>
- Antonellini, M. A., & Pollard, D. D. (1995). Distinct element modeling of deformation bands in sandstone. *Journal of Structural Geology*, 17(8), 1165–1182. [https://doi.org/10.1016/0191-8141\(95\)00001-T](https://doi.org/10.1016/0191-8141(95)00001-T)
- Azéma, E., & Radjai, F. (2014). Internal structure of inertial granular flows. *Physical Review Letters*, 112(7), 1–5. <https://doi.org/10.1103/PhysRevLett.112.078001>
- Berger, N., Azéma, E., Douce, J. F., & Radjai, F. (2015). Scaling behaviour of cohesive granular flows. *Epl*, 112(6). <https://doi.org/10.1209/0295-5075/112/64004>
- Biegel, R. L., Sammis, C. G., & Dieterich, J. H. (1989). The frictional properties of a simulated gouge having a fractal particle distribution. *Journal of Structural Geology*, 11(7), 827–846. [https://doi.org/10.1016/0191-8141\(89\)90101-6](https://doi.org/10.1016/0191-8141(89)90101-6)
- Billi, A. (2005). Grain size distribution and thickness of breccia and gouge zones from thin (<1 m) strike-slip fault cores in limestone. *Journal of Structural Geology*, 27(10), 1823–1837.
<https://doi.org/10.1016/j.jsg.2005.05.013>
- Billi, A., & Storti, F. (2004). Fractal distribution of particle size in carbonate cataclastic rocks from the core of a regional strike-slip fault zone. *Tectonophysics*, 384(1–4), 115–128.
<https://doi.org/10.1016/j.tecto.2004.03.015>
- Bishop, A. W. (1971). The Influence of Progressive Failure on the Choice of the Method of Stability Analysis. *Géotechnique*, 21(2), 168–172. <https://doi.org/10.1680/geot.1971.21.2.168>
- Blenkinsop, T. G. (1991). Cataclasis and Processes of Particle Size Reduction. *Pure and Applied Geophysics*,

136(1), 59–86. <https://doi.org/10.1007/BF00878888>

Byerlee, J. D., & Brace, W. F. (1968). Stick slip, stable sliding, and earthquakes-Effect of rock type, pressure, strain rate, and stiffness. *Journal of Geophysical Research*, 73(18), 6031–6037.

<https://doi.org/10.1029/JB073i018p06031>

850 Byerlee, J. D., & Savage, J. C. (1992). Coulomb plasticity within the fault zone. *Geophysical Research Letters*, 19(23), 2341–2344. <https://doi.org/10.1029/92GL02370>

Cho, N., Martin, C. D., & Sego, D. C. (2007). A clumped particle model for rock. *International Journal of Rock Mechanics and Mining Sciences*, 44(7), 997–1010. <https://doi.org/10.1016/j.ijrmms.2007.02.002>

Cho, N., Martin, C. D., & Sego, D. C. (2008). Development of a shear zone in brittle rock subjected to direct
855 shear. *International Journal of Rock Mechanics and Mining Sciences*, 45(8), 1335–1346.

<https://doi.org/10.1016/j.ijrmms.2008.01.019>

Cundall, P. A. ., & Strack, O. D. L. (1979). A discrete numerical model for granular assemblies. *Géotechnique*, 29(1), 47–65. <https://doi.org/10.1680/geot.1979.29.1.47>

Da Cruz, F., Emam, S., Prochnow, M., Roux, J. N., & Chevoir, F. (2005). Rheophysics of dense granular
860 materials: Discrete simulation of plane shear flows. *Physical Review E*, 72(2), 1–17.

<https://doi.org/10.1103/PhysRevE.72.021309>

Daouadji, A., & Hicher, P. (2010). An enhanced constitutive model for crushable granular materials. *International Journal for Numerical and Analytical Methods in Geomechanics*, 34, 555–580.

<https://doi.org/10.1002/nag>

865 Daouadji, A., Hicher, P., Rahma, A., Daouadji, A., Hicher, P., & Rahma, A. (2001). An elastoplastic model for granular materials taking into account grain breakage. *European Journal of Mechanics - A/Solids*, 20(1), 113–137. [https://doi.org/10.1016/S0997-7538\(00\)01130-X](https://doi.org/10.1016/S0997-7538(00)01130-X)

Das, A., Tengattini, A., Nguyen, G. D., Viggiani, G., Hall, S. A., & Einav, I. (2014). A thermomechanical constitutive model for cemented granular materials with quantifiable internal variables. Part II - Validation
870 and localization analysis. *Journal of the Mechanics and Physics of Solids*, 70(1), 382–405.

<https://doi.org/10.1016/j.jmps.2014.05.022>

Di Toro, Giulio, Hirose, T., Nielsen, S., Pennacchioni, G., & Shimamoto, T. (2006). Natural and Experimental Evidence of Melt Lubrication of Faults During Earthquakes. *SCIENCE*, 311(5761), 647–649.

<https://doi.org/10.1126/science.1121012>

875 Dorostkar, O., Guyer, R. A., Johnson, P. A., Marone, C., & Carmeliet, J. (2017). On the role of fluids in stick-slip dynamics of saturated granular fault gouge using a coupled computational fluid dynamics-discrete element approach. *Journal of Geophysical Research: Solid Earth*, 122(5), 3689–3700.

<https://doi.org/10.1002/2017JB014099>

Dunn, D. E., LaFountain, L. J., & Jackson, R. E. (1973). Porosity Dependence and Mechanism of Brittle
880 Fracture in Sandstones. *Journal of Geophysical Research*, 78(14).

<https://doi.org/10.1029/JB078i014p02403>

Estrada, N., Lizcano, A., & Taboada, A. (2010). Simulation of cemented granular materials. I. Macroscopic stress-strain response and strain localization. *Physical Review E*, 82, 1–11.

<https://doi.org/10.1103/PhysRevE.82.011303>

885 Faqih, A., Chaudhuri, B., Muzzio, F. J., Tomassone, M. S., & Hammond, S. (2006). *Flow - Induced Dilation of*

Cohesive Granular Materials. 52(12). <https://doi.org/10.1002/aic>

Ferdowsi, B. (2014). *Discrete element modeling of triggered slip in faults with granular gouge Application to dynamic earthquake triggering* [ETH Zurich]. <https://doi.org/10.3929/ethz-a-010232908>

Fillot, N., Iordanoff, I., & Berthier, Y. (2007). *Wear modeling and the third body concept*. 262, 949–957.

<https://doi.org/10.1016/j.wear.2006.10.011>

Friedman, M., Handin, J., & Alani, G. (1972). Fracture-surface energy of rocks. *International Journal of Rock Mechanics and Mining Sciences & Geomechanics*, 9(6), 757–764. [https://doi.org/10.1016/0148-9062\(72\)90034-4](https://doi.org/10.1016/0148-9062(72)90034-4)

Frye, K. M., & Marone, C. (2003). The effect of particle dimensionality on Granular friction in laboratory shear zones. *Geophysical Research Letters*, 29(19), 22-1-22–24. <https://doi.org/10.1029/2002gl015709>

Gao, K., Euser, B. J., Rougier, E., Guyer, R. A., Lei, Z., Knight, E. E., Carmeliet, J., & Johnson, P. A. (2018). Modeling of Stick-Slip Behavior in Sheared Granular Fault Gouge Using the Combined Finite-Discrete Element Method. *Journal of Geophysical Research: Solid Earth*, 123(7), 5774–5792.

<https://doi.org/10.1029/2018JB015668>

GRD Midi. (2004). On dense granular flows. *European Physical Journal E*, 14(4), 341–365.

<https://doi.org/10.1140/epje/i2003-10153-0>

Guo, Y., & Morgan, J. K. (2004). Influence of normal stress and grain shape on granular friction: Results of discrete element simulations. *Journal of Geophysical Research: Solid Earth*, 109(B12).

<https://doi.org/10.1029/2004JB003044>

Handin, J. (1969). On the Coulomb-Mohr Failure Criterion. *Journal of Geophysical Research*, 74(22), 5343–5348. <https://doi.org/10.1029/JB074i022p05343>

Hirth, G., & Tullis, J. (1989). The effects of pressure and porosity on the micromechanics of the brittle-ductile transition in quartzite. *Journal of Geophysical Research*, 94(B12).

<https://doi.org/10.1029/jb094ib12p17825>

Iordanoff, I., Fillot, N., & Berthier, Y. (2005). Numerical study of a thin layer of cohesive particles under plane shearing. *Powder Technology*, 159(1), 46–54. <https://doi.org/10.1016/j.powtec.2005.05.053>

Jaeger, J. C. (1971). Friction of rocks and stability of slopes. *Geotechniques*, 116(4–5), 615–626.

<https://doi.org/10.1007/BF00876528>

Jiang, M., Zhang, W., Sun, Y., & Utili, S. (2013). An investigation on loose cemented granular materials via DEM analyses. *Granular Matter*, 15(1), 65–84. <https://doi.org/10.1007/s10035-012-0382-8>

Kasyap, S. S., & Senetakis, K. (2020). An Experimental Investigation on the Tribological Behaviour of Nominally Flat Quartz Grains with Gouge Material in Dry, Partial Saturated and Submersed Conditions. *Pure and Applied Geophysics*. <https://doi.org/10.1007/s00024-020-02431-1>

Kranz, R. L., & Scholz, C. H. (1977). *Critical Dilatant Volume of Rocks at the Onset of Tertiary Creep crack observation using the scanning electron microscope each quartzite*. 82(30).

<https://doi.org/10.1029/JB082i030p04893>

Lade, P. V., & Overton, D. D. (1989). Cementation Effects in Frictional Materials. *Journal of Geotechnic Engineering*, 115(10), 1373–1387. [https://doi.org/10.1061/\(ASCE\)0733-9410\(1989\)115:10\(1373\)](https://doi.org/10.1061/(ASCE)0733-9410(1989)115:10(1373))

Lin, A. (1999). S-C cataclasite in granitic rock. *Tectonophysics*, 304(3), 257–273. [https://doi.org/10.1016/S0040-1951\(99\)00026-8](https://doi.org/10.1016/S0040-1951(99)00026-8)

- Lockner, D. A., & Beeler, N. M. (2002). Rock failure and Earthquakes. *International Geophysics Series*, 81(A), 505–538.
- Mair, K., Frye, K. M., & Marone, C. (2002). Influence of grain characteristics on the friction of granular shear zones. *Journal of Geophysical Research: Solid Earth*, 107(B10), ECV 4-1-ECV 4-9.
 930 <https://doi.org/10.1029/2001JB000516>
- Mair, K., & Marone, C. (1999). Friction of simulated fault gouge for a wide range of velocities and normal stresses. *Journal of Geophysical Research: Solid Earth*, 104(B12), 28899–28914.
<https://doi.org/10.1029/1999JB900279>
- Majmudar, T. S., & Behringer, R. P. (2005). *Contact force measurements and stress-induced anisotropy in granular materials*. 435(June), 1079–1082. <https://doi.org/10.1038/nature03805>
 935
- Marone, C. (1995). Fault zone strength and failure criteria. *Geophysical Research Letters*, 22(6), 723–726.
<https://doi.org/10.1029/95GL00268>
- Marone, C. (1998). Laboratory-derived friction laws and their application to seismic faulting. *Annual Review of Earth Planetary Sciences*, 26, 643–696.
- 940 Marone, C., Hobbs, B. E., & Ord, A. (1992). Coulomb Constitutive Laws for Friction : Contrasts in Frictional Behavior for Distributed and Localized Shear. *Pageoph*, 139(2). <https://doi.org/10.1007/BF00876327>
- Marone, C., & Kilgore, B. (1993). Scaling of the critical slip distance for seismic faulting with shear strain in fault zones. *Letters to Nature*, 362, 210–211. <https://doi.org/10.1038/362618a0>
- Marone, C., & Scholz, C. H. (1988). The depth of seismic faulting and the upper transition from stable to
 945 unstable slip regimes. *Geophysical Research Letters*, 15(8), 621–624.
<https://doi.org/10.1029/GL015i006p00621>
- Marone, C., & Scholz, C. H. (1989). Particle-size distribution and microstructures within simulated fault gouge. *Journal of Structural Geology*, 11(7), 799–814. [https://doi.org/10.1016/0191-8141\(89\)90099-0](https://doi.org/10.1016/0191-8141(89)90099-0)
- Maurer, W. C. (1965). Shear Failure of Rock Under Compression. *SPE J.*, 5, 167–176.
 950 <https://doi.org/10.2118/1054-PA>
- Mead, W. J. (1925). The Geologic Rôle of Dilatancy. *The Journal of Geology*, 33(7), 685–698.
<https://doi.org/10.1086/623241>
- Misra, S., Mandal, N., & Chakraborty, C. (2009). Formation of Riedel shear fractures in granular materials : Findings from analogue shear experiments and theoretical analyses. *Tectonophysics*, 471(3–4), 253–259.
 955 <https://doi.org/10.1016/j.tecto.2009.02.017>
- Mollon, G. (2016). A multibody meshfree strategy for the simulation of highly deformable granular materials. *International Journal for Numerical Methods in Engineering*, 108(12), 1477–1497.
<https://doi.org/10.1002/nme.5258>
- Mollon, G. (2018a). A unified numerical framework for rigid and compliant granular materials. *Computational Particle Mechanics*, 5, 517–527. <https://doi.org/10.1007/s40571-018-0187-6>
 960
- Mollon, G. (2018b). Mixtures of hard and soft grains: micromechanical behavior at large strains. *Granular Matter*, 20(39). <https://doi.org/10.1007/s10035-018-0812-3>
- Mollon, G., Quacquarelli, A., Andò, E., & Viggiani, G. (2020). Can friction replace roughness in the numerical simulation of granular materials? *Granular Matter*, 22(42). <https://doi.org/10.1007/s10035-020-1004-5>
- 965 Mollon, G., & Zhao, J. (2012). Fourier-Voronoi-based generation of realistic samples for discrete modelling of

- granular materials. *Granular Matter*, 5, 621–638. <https://doi.org/10.1007/s10035-012-0356-x>
- Morgan, J. K. (1999). Numerical simulations of granular shear zones using the distinct element method: 2. Effects of particle size distribution and interparticle friction on mechanical behavior. *Journal of Geophysical Research: Solid Earth*, 104(B2), 2721–2732. <https://doi.org/10.1029/1998jb900055>
- 970 Morgan, J. K., & Boettcher, M. S. (1999). Numerical simulations of granular shear zones using the distinct element method: 1. Shear zone kinematics and the micromechanics of localization. *Journal of Geophysical Research: Solid Earth*, 104(B2), 2703–2719. <https://doi.org/10.1029/1998jb900056>
- Muto, J., Nakatani, T., Nishikawa, O., & Nagahama, H. (2015). Fractal particle size distribution of pulverized fault rocks as a function of distance from the fault core. *Geophysical Research Letters*, 42(10), 3811–3819. <https://doi.org/10.1002/2015GL064026>
- 975 <https://doi.org/10.1002/2015GL064026>
- Niemeijer, A., Toro, G. Di, Nielsen, S., & Felice, F. Di. (2011). Frictional melting of gabbro under extreme experimental conditions of normal stress, acceleration, and sliding velocity. *Journal of Geophysical Research*, 116(B07404). <https://doi.org/10.1029/2010JB008181>
- Noel, C., Passelègue, F. X., & Violay, M. (2021). Brittle faulting of ductile rock induced by pore fluid pressure build-up. *Journal of Geophysical Research*. <https://doi.org/10.1029/2020JB021331>
- 980 <https://doi.org/10.1029/2020JB021331>
- Nouguier-lehon, C., Cambou, B., & Vincens, E. (2003). Influence of particle shape and angularity on the behaviour of granular materials : a numerical analysis. *International Journal for Numerical and Analytical Methods in Geomechanics*, 27(14), 1207–1226. <https://doi.org/10.1002/nag.314>
- Olgaard, D. L., & Brace, W. F. (1983). The microstructure of gouge from a mining-induced seismic shear zone. *International Journal of Rock Mechanics and Mining Sciences & Geomechanics*, 20(1), 11–19. [https://doi.org/10.1016/0148-9062\(83\)91610-8](https://doi.org/10.1016/0148-9062(83)91610-8)
- 985 [https://doi.org/10.1016/0148-9062\(83\)91610-8](https://doi.org/10.1016/0148-9062(83)91610-8)
- Paglialunga, F., Passelègue, F., Brantut, N., Barras, F., Lebihain, M., & Violay, M. (2021). On the scale dependence in the dynamics of frictional rupture : constant fracture energy versus size-dependent breakdown work. *Preprint in Earth and Planetary Science Letters*, 1–33.
- 990 Philit, S., Soliva, R., Castilla, R., Ballas, G., & Taillefer, A. (2018). Clusters of cataclastic deformation bands in porous sandstones. *Journal of Structural Geology*, 114, 235–250. <https://doi.org/10.1016/j.jsg.2018.04.013>
- Potyonody, D. O., & Cundall, P. A. (2004). A bonded-particle model for rock. *International Journal of Rock Mechanics and Mining Sciences*, 41(8), 1329–1364. <https://doi.org/10.1016/j.ijrmms.2004.09.011>
- Rathbun, A. P., Renard, F., & Abe, S. (2013). Numerical investigation of the interplay between wall geometry and friction in granular fault gouge. *Journal of Geophysical Research: Solid Earth*, 118(3), 878–896. <https://doi.org/10.1002/jgrb.50106>
- 995 <https://doi.org/10.1002/jgrb.50106>
- Rice, J., & Cocco, M. (2002). Seismic Fault Rheology and Earthquake Dynamics. *Journal of Geophysical Research*, 107, 1000–1029.
- Rice, J. R. (2006). Heating and weakening of faults during earthquake slip. *Journal of Geophysical Research: Solid Earth*, 111(5), 1–29. <https://doi.org/10.1029/2005JB004006>
- 1000 <https://doi.org/10.1029/2005JB004006>
- Rognon, P. G., Roux, J. N., Naaïm, M., & Chevoir, F. (2008). Dense flows of cohesive granular materials. *Journal of Fluid Mechanics*, 596, 21–47. <https://doi.org/10.1017/S0022112007009329>
- Roy, S., & Luding, S. (2017). Effect of cohesion on local compaction and granulation of sheared soft granular materials. *Powders&Grains*, 03065, 2–5. <https://doi.org/10.1051/epjconf/201714003065>
- 1005 Sammis, C. G., & Biegel, R. L. (1989). Fractals, Fault-Gouge, and Friction. *Pure and Applied Geophysics*, 131,

255–271. <https://doi.org/10.1007/BF00874490>

Sammis, C., King, G., & Biegel, R. (1987). The kinematics of gouge deformation. *Pure and Applied Geophysics*, 125, 777–812. <https://doi.org/10.1007/BF00878033>

Sandeep, C. S., & Senetakis, K. (2019). An experimental investigation of the microslip displacement of geological materials. *Computers and Geotechnics*, 107(June 2018), 55–67. <https://doi.org/10.1016/j.compgeo.2018.11.013>

Schellart, W. P. (2000). Shear test results for cohesion and friction coefficients for different granular materials : scaling implications for their usage in analogue modelling. *Tectonophysics*, 324(1–2), 1–16. [https://doi.org/10.1016/S0040-1951\(00\)00111-6](https://doi.org/10.1016/S0040-1951(00)00111-6)

Taylor, D. W. (1948). *Fundamentals of Soil Mechanics* (J. W. & Sons (ed.)). London - CHAPMAN & HALL, Limited.

Tchalenko, J. S. (1970). Similarities between shear zones of different magnitudes. *Geological Society Of America Bulletin*, 81(6), 1625–1640. [https://doi.org/10.1130/0016-7606\(1970\)81\[1625:SBSZOD\]2.0.CO;2](https://doi.org/10.1130/0016-7606(1970)81[1625:SBSZOD]2.0.CO;2)

Tengattini, A., Das, A., Nguyen, G. D., Viggiani, G., Hall, S. A., & Einav, I. (2014). A thermomechanical constitutive model for cemented granular materials with quantifiable internal variables. Part I - Theory. *Journal of the Mechanics and Physics of Solids*, 70(1), 281–296. <https://doi.org/10.1016/j.jmps.2014.05.021>

Toro, G Di, Han, R., Hirose, T., Paola, N. De, Nielsen, S., Mizoguchi, K., Ferri, F., Cocco, M., & Shimamoto, T. (2011). Fault lubrication during earthquakes. *Nature*, 471, 494–498. <https://doi.org/10.1038/nature09838>

Wissa, A. E. Z. (1965). *Effective stress-strength behavior of cemented soils (Thesis (Sc D.))*. Massachusetts institute of technology.

Wood, D. M. (1990). *Soil behaviour and critical state soil Mechanics* (Cambridge university Press (ed.)). <https://doi.org/10.1201/9781351255400-1>

Zhang, L., Nguyen, N. G. H., Lambert, S., Nicot, F., Prunier, F., & Djeran-Maigre, I. (2017). The role of force chains in granular materials: from statics to dynamics. *European Journal of Environmental and Civil Engineering*, 21(7–8), 874–895. <https://doi.org/10.1080/19648189.2016.1194332>

Zhao, Z., Jing, L., & Neretnieks, I. (2012). Particle mechanics model for the effects of shear on solute retardation coefficient in rock fractures. *International Journal of Rock Mechanics and Mining Sciences*, 52, 92–102. <https://doi.org/10.1016/j.ijrmms.2012.03.001>